Aerodynamic Inverse Design of Multistage Turbomachinery Blading

Benedikt Roidl

A Thesis

in

The Department

of

Mechanical and Industrial Engineering

Presented in Partial Fulfillment of the Requirements

for the Degree of Master of Applied Science (Mechanical Engineering) at

Concordia University

Montréal, Québec, Canada

Mai 2008

ABSTRACT

Aerodynamic Inverse Design of Multistage Turbomachinery Blading

Benedikt Roidl

A recently developed inverse method for single blade rows is extended to 2-D and quasi 3-D multi-stage application. In that method, the pressure distribution on the blade surfaces or alternatively, the blade loading and their thickness distribution are specified and the blade shape is sought using a virtual wall movement. The blade walls move with a virtual velocity distribution that is derived from the difference between the current and the target pressure distribution on the blade surfaces. The scheme is fully consistent with the viscous flow assumption and it is implemented into the time accurate solution of the Reynolds-Averaged Navier-Stokes equations that are expressed in an arbitrary Lagrangian-Eulerian (ALE) form to account for mesh movement. A cell-vertex finite volume method of the Jameson type is used to discretize the equations in space; time accurate integration is obtained using dual time stepping. An algebraic Baldwin-Lomax turbulence model is used for turbulence closure. In order to extend the present method to multistage applications a mixing plane approach using flux averaged flow conditions is employed to couple the vane (stator) and blade (rotor) regions and non-reflecting boundary conditions are implemented at the interface between the two regions to account for short distances between blade leading and trailing edges and the corresponding inlet and exit boundaries. The method is validated on two different cases. Finally three different stages are redesigned: The E/TU-3 single stage turbine, the E/TU-4 2.5 stage turbine and the E/CO-5 2.5 stage compressor. For all cases presented in this thesis the blade pressure distributions and pressure loadings, respectively were selected as design variables, and, by modifying the original profile, it was possible to improve the aerodynamic performance.

ACKNOWLEDGEMENTS

I would like to express my gratitude to my thesis supervisor, Professor Ghaly, for his guidance, enthusiasm, interesting talks and inspiring mind during the course of this masters.

I also thank my colleagues Raja Ramamurthy and Mohammad Arabnia for their support, advice and company in unnumbered late night lab sessions.

Special thanks to the staff of the MIE department, for their support, especially at the beginning of my masters but also throughout my entire stay.

Finally I thank my girlfriend, Andrea, for her patience and love over the months in which she has not been in Montreal but waiting far away in Germany for my return.

TABLE OF CONTENTS

LIST OF FIGURES

LIST OF TABLES

LIST OF SYMBOLS

A	Auxiliary matrix
c	Speed of sound
D	Dissipative and body force terms
DF	Diffusion coefficient
e	Total energy
F	Conservative flux vector, virtual momentum flux
G	Viscous flux vector
h	Stream tube thickness
H	Total enthalpy
i, j, k	Counter
K	Eigenvalue matrix of characteristic method
$\dot{m}$	Mass flow rate
M	Mach number
n	Normal vector
N	Number of nodes at inlet and exit boundary
p	Pressure
Q	Discrete approximation to convective fluxes
Pr	Prandtl number
R	Gas constant, Residual vector
s	Wall displacement
S	Source term related to quasi 3-D
T	Temperature
t	Fictitious or physical time
U	Conservative variable vector
u	Velocity in axial direction
v	Velocity in circumferential direction
w	Velocity

α	Inlet flow angle
β	Damping coefficient
ϵ	Under-relaxation factor for wall movement
Γ	Cell surface
τ	Stress tensor
σ	Under-relaxation factor for local characteristic changes
λ	Stokes relation
η	Efficiency
δ	Kronecker delta, changes in characteristics
ρ	Density
γ	Specific heat ratio, damping coefficient
Ω	Control volume
ζ	Loss coefficient
μ	Dynamic viscosity
ϕ	Characteristic variable
ξ	Stagger angle
θ	Chamber angle
ϕ, ξ	Mesh coordinates

Subscripts

0	Total quantity
e	Cell edge related
ex	Extrapolated from interior domain
F	Flux average value
$isen$	Isentropic
new	Recent fictitious time step
old	Old fictitious time step
p	Primitive variables
$rotor$	Rotor blade row
$stator$	Stator blade row
$t-t$	Total-to-total efficiency

x	Axial direction
y	Circumferential direction

Superscripts

$-$	Suction side
$+$	Pressure side
d	Design quantity
v	Virtual quantity

Acronyms

CFL	Courant number
CFD	Computational Fluid Dynamics.
IGV	Inlet Guide Vane
LE	Leading edge
NRBC	Non-reflecting boundary conditions.
RANS	Reynolds number Averaged Navier-Stokes
R(1,2)	Rotor
S(1,2)	Stator
TE	Trailing edge

Chapter 1

Introduction

Today, inverse design methods are used for many engineering problems and design cases. One application among them is, in combination with CFD techniques, to guide and support the aerodynamic design of turbomachine blades. Although CFD analysis methods evolved rapidly in the last decades, the development of aerodynamic design tools have not improved that fast. Many designers who work in the field of turbomachinery still use CFD analysis tools in combination with their own design experience to shape a blade. The time factor as well as the resulting design efficiency might suffer from these traditional design approaches.

There are sophisticated design methodologies that a designer can use to improve the performance of single blade rows or even multistage applications. One of them is automatic numerical optimization [1, 2, 3], where blade geometry parameters of a single blade row or entire stages [4] are iteratively modified to satisfy a particular objective function. These functions are computed using CFD flow simulations. The major advantage of a numerical optimization method is its flexibility in implementing it in (or combing it with) any type of flow solver and objective function. However, they are computationally very expensive as a great number of flow simulations is needed to obtain results which satisfy the objective function. Thus, numerical simulations

are generally appropriate for design cases where a detailed target performance is not known and where an optimum performance constitutes the sole goal. However, in cases where this mentioned target performance is already known, e.g., target pressure loading or pressure distributions on the blade surfaces, the inverse design method constitutes the most appropriate approach for aerodynamic design. In an inverse shape design problem, the flow governing equations are written in a form that would give the blade shape, that produces a detailed target performance as well as the flow field, simultaneously. The time that the redesign process with an inverse method would take is of the order of one to five analysis runs. Therefore this method is more time efficient than most numerical optimization approaches.

The main object of this work is to extend the existing inverse method from single blade application to multistage applications. The present code is modified to accommodate additional fields in boundary conditions and restructuring the whole approach for establishing inverse design process for multistage turbomachine blades.

1.1. Inverse design approach

An alternative to an analysis approach, where the performance of a given blade is calculated from the flow governing equations, constitutes the inverse shape design. There, the performance of a blade is prescribed and the corresponding geometry is obtained as part of the flow solution. The main goal of an inverse design process is to achieve a blade shape which is satisfying a particular target quantity, while the computational time remains comparable to the corresponding flow analysis. Although inverse design is used in industry it is still far from being considered as sophisticated as analysis methods.

1.1.1 Previous investigations

Ordinarily, two-dimensional inverse blade design methods assume a target distribution along the blade surfaces, be it pressure [5, 6, 7, 8, 9], Mach number [10], or velocity [11]. Other inverse methods assume a target distribution of the blade pressure loading and its thickness distribution [12, 13, 14, 15]. Starting from an initial guess for the blade shape, these methods use a flow analysis tool to compute the flow field, then the difference between the calculated and the target e.g. pressure distribution on the blade surfaces is used to change the blade shape and the process is repeated until convergence.

Some inverse blade design methods for viscous flows were shown to be quite efficient [7, 8, 13, 15, 9], however they still carry some traces of inviscid flow implementation. Some methods [7] involve viscous-inviscid interaction (so that the metal profile has to be obtained by subtracting the displacement thickness), some [13, 15] use the tangency condition to find the new blade camber line, while other methods [8] use the transpiration approach where a velocity tangent to the blade is needed. The most recent approach of de Vito *et al.* [9] consists of blending a Navier-Stokes solver, for the flow analysis, with an Euler solver for the inverse design. In all the preceding methods, it is assumed that the flow is attached and the boundary layers are well behaved, so that the velocity at the edge of the boundary layer can be used to get the new blade profile. A recent example of the use of inverse methods in the design of multistage compressor to improve stage matching is given in van Rooij *et al.* [16], which is based on the work of Dang [12, 13]

Most inverse design methods solve the problem as a time-marching (quasi-steady) problem and do not account for the blade movement in the problem formulation. The errors resulting from the quasi-steady assumption will propagate into the new blade shape which will affect the pressure field computed at the next iteration. In some design approaches and for some target pressure distributions, such

errors can result in an inaccurate blade shape or in the divergence of the iterative process. A possible example of this situation is the work of Yang and Ntone [17], who extended the work of Thompkins and Tong [5, 18] to viscous flow, where the blade shape obtained for subsonic viscous flow was rather wavy. Moreover that approach [17] was not successful in designing transonic blades. The elimination of these errors by using a time accurate formulation will result in a more robust method that can handle relatively 'difficult' design cases. This fact is verified in part by Demeulenaere *et al.* [8] who used a time marching (but not time accurate) approach where they accounted for the mesh movement into the formulation, thus improving the convergence of the inverse method. The merits of using a time accurate solution on a moving mesh were demonstrated by Daneshkhah and Ghaly [19] who showed that the conventional quasi-steady formulation fails to converge for two cases out of three where the time accurate formulation converged without any problems.

Daneshkhah and Ghaly [19, 20, 21] presented an inverse blade design method [20, 19] that is fully consistent with the viscous flow assumption, and used it in the redesign of the VKI-LS89 transonic turbine vane [21]. The main features of that inverse method are: a- The blade walls move with a virtual velocity distribution derived from the difference between the current and the target pressure distributions on the blade surfaces; b- The method is implemented into the time accurate solution of the Reynolds-Averaged Navier-Stokes (RANS) equations, written for a moving and deforming computational domain. An inverse design approach similar to that of Daneshkhah and Ghaly [20, 19] was independently developed by Mileshin *et al.* [22] and was used in the 3D inverse design of a transonic fan rotor.

1.1.2   Present investigations

In this work, the method developed by Daneshkhah and Ghaly [20, 19] which was applied to the redesign of a single 2D blade row, is extended to handle one or more

4

stages in two-dimensional flow. The stator-rotor interaction is based on the steady mixing plane model advanced by Giles [23]. The NRBC, developed by Giles [24] and Chima [25], respectively, were implemented at the mixing planes that are located at the interface between any two blade regions where flow inlet and exit boundary conditions are applied to ensure a proper communication of mass, momentum and energy fluxes.

1.2. Flow analysis in turbomachines

Powerful 3D-Reynolds-Averaged-Navier-Stokes (RANS) solver are widely available and are able to capture the challenging flow behavior which is occurring in a turbomachine passage. Most of the flow pattern in turbine or compressor blades have a three dimensional nature and therefore 3D solver are needed to capture these effects. Some amongst others are endwall-, tip, corner separations or secondary flows. Figure 1.1 and 1.2 shows a compilation of flow characteristics in a 3D blade passage of a compressor and a turbine, respectively. Unsteady effects such as rotor/stator interaction, stalled flows, or flutter also contribute to the flow complexity.

Within the last two decades turbomachinery CFD has evolved from isolated blade row methods to hierarchical multistage analysis in order to simulate the mentioned flow physics in multistage compressors and turbines [12, 26, 27, 28]. These codes apply a time accurate solution of the unsteady Navier-Stokes equations. The grid is partitioned into stationary parts for the stator sections and moving/rotating grids for the rotor sections. Steady/unsteady inflow and outflow boundaries are modeled using quasi 3D or fully 3D non-reflecting boundary conditions (NRBC), while flux averaged mixing plane models are mainly used [26, 25] to model the steady state rotor-stator interaction. Unsteady blade row coupling schemes get more interesting with the advent of more powerful CPUs and parallelization methods. Moving grids

5

have excelled at any type of unsteady calculation such as stator/rotor interaction [29], dynamic response predictions of stall flutter [30], aeroelastic [31] or mistuning effects [32].

As efficient mixing plane models were introduced at the same time where 3D CFD codes became computationally affordable there are not many 2D CFD codes which account for a multistage environment [24]. Furthermore, there is not much useful data provided to assess 2D multistage codes as present turbomachinery stages have aspect ratios of about 1.5 - 3 which of course push 3D effects more in the spotlight.

Nevertheless, interesting investigations can still be made in a 2D multistage turbomachine such as aerodynamic matching studies or coupled inverse design. Typical flow phenomena of turbomachines are exhibited in 2D flow, i.e. shock waves and their interaction with boundary layers and wakes or flow separation. Furthermore, compared to their 3D counterparts, 2D flow analysis is computationally cheap, and hence reasonably fast, but yet it provides accurate simulation results. Furthermore, when extended to quasi 3D, major 1D flow effects caused by flaring annulus geometries and endwall boundary layer growth. 2D simulations are also an imperative design step to take before going to the 3D flow simulation.

1.2.1 Present analysis method

In the present work, the Reynolds-averaged Navier-Stokes (RANS) equations are used to describe the flow field both in the analysis and design modes of the computations. The Baldwin-Lomax model [33], adapted for the use on unstructured meshes [34] is used for turbulence closure. The governing equations are written for unsteady flow in a domain with moving and deforming boundaries using an Arbitrary Lagrangian-Eulerian (ALE) formulation. The spatial discretization of the governing equations is performed using a second order cell-vertex Finite Volume (FV) method of Jameson's
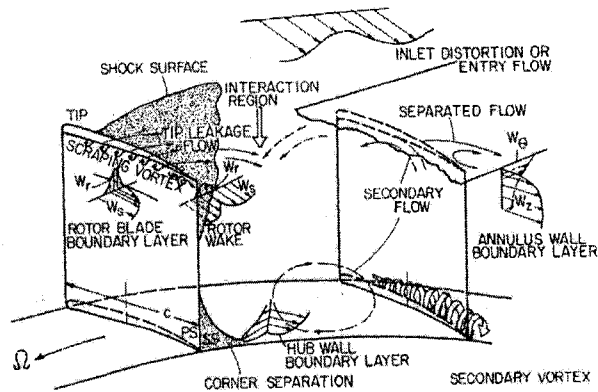
Abbildung 1.1: Flow characteristics in a compressor blade row [taken from Lakshmi-narayana [38]]

type on a fully unstructured triangular mesh [35]. The method uses an explicit Runge-Kutta pseudo-time stepping procedure to obtain the stationary solution where local pseudo-time stepping and implicit residual smoothing are employed for convergence acceleration. During the design process, a time accurate solution is ensured using a dual time stepping scheme [36]. The grid velocities for a moving mesh are computed from the space conservation law (SCL) [37]. The flux averaged mixing plane approach [23] was introduced to couple the successive blade rows and non-reflecting boundary conditions [24] were imposed at inflow, outflow and at the mixing plane(s).

In this mixing plane, the conservation variables are averaged over one pitch and the resulting flux averaged variables are conserved across the mixing plane, as suggested by Giles [23]. Although this approach is known to generate slightly higher losses in the averaging procedure compared with other methods, it was used since it conserves all fluxes across the mixing plane.

In a turbomachinery stage, the gap between stator trailing edge and rotor leading edge is normally less then 25% axial chord, therefore NRBC, introduced by Giles [24], were implemented. They reduce the magnitude of the nonphysical wave reflections at the mixing plane by employing a discrete Fourier transform to take into account
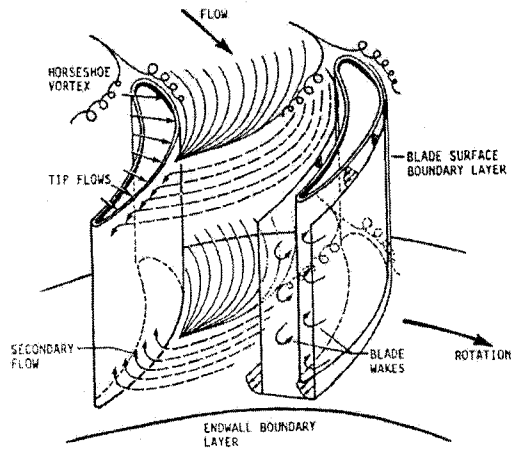
Abbildung 1.2: Flow characteristics in a turbine blade row [courtesy of NASA-Lewis Research Center]

the local changes in the characteristic variables that are updated with each time step. Another approach, which was introduced by Chima [25], was also implemented and used as it showed an advantageous behavior in applications where several stages were simulated simultaneously. Both approaches are detailed in Chapter 2 and validated in Appendix B.

1.2.2 Mesh considerations

Structured and unstructured grids have both their advantages and disadvantages when applied in internal flow methods. In 3D computations there is an increased demand of computational power when unstructured grids are used to represent the flow domain. However, in order to properly model complex geometry features such as thick LE/TE sections, cooling holes, etc. unstructured grids present an advantageous choice compared to structured grids in internal flows. Unstructured grids, too, can be easily coupled with mesh adaptation routines to satisfy increased standards in efficiency and accuracy.

In the present code a sheared H-mesh as well as a hybrid mesh were used to model different flow cases. The hybrid mesh consists of two different types of grids; an O-mesh near the blade surface where large aspect ratios are required to resolve properly the boundary layer behavior near the blade, this mesh blends into a Delauny mesh that fills the rest of the computational domain. The hybrid mesh delivers very good results for viscous flows and is superior compared to an H-mesh in terms of convergence and accuracy. Figure 1.3 depicts a hybrid grid around the blades of a 2.5 stage compressor.

1.3. Thesis outline

This thesis consists of five chapters including the introduction. The second chapter presents the numerical implementation of various mixing plane models, NRBC and quasi-three-dimensional effects. Chapter three discusses the inverse design formulation and its implementation and it discusses the different choices of design variables as well as general design considerations. The design method is validated for a rotor blade in a hypothetical subsonic turbine environment and the stator blade of the E/TU-3 turbine. Chapter four presents the application of the design method to different turbine and compressor stage cases. First, the E/TU-3 turbine is redesigned to increase the efficiency level by modifying different performance aspects. The second case investigates a 2.5-stage E/TU-4 turbine where a parallel redesign of two blades was performed. The last case consists of a 2.5 stage E/CO-5 subsonic compressor where three blades were redesigned in order to improve the overall performance of the compressor stages. These three cases demonstrate the usefulness and practicality of the method. The final chapter concludes the thesis by summarizing the main achievements and providing recommendations for future work. The main text is followed by several appendices that complement the work. Appendix A gives a validation on

the quasi-three dimensional flow and Appendix B reviews the different approaches of the NRBC. Appendix C denotes to the validation of the multistage code where an E/TU-3 single stage turbine and an E/TU-4 multistage turbine are analyzed. In Appendix D the implementation of time-accurate RANS equations is presented.
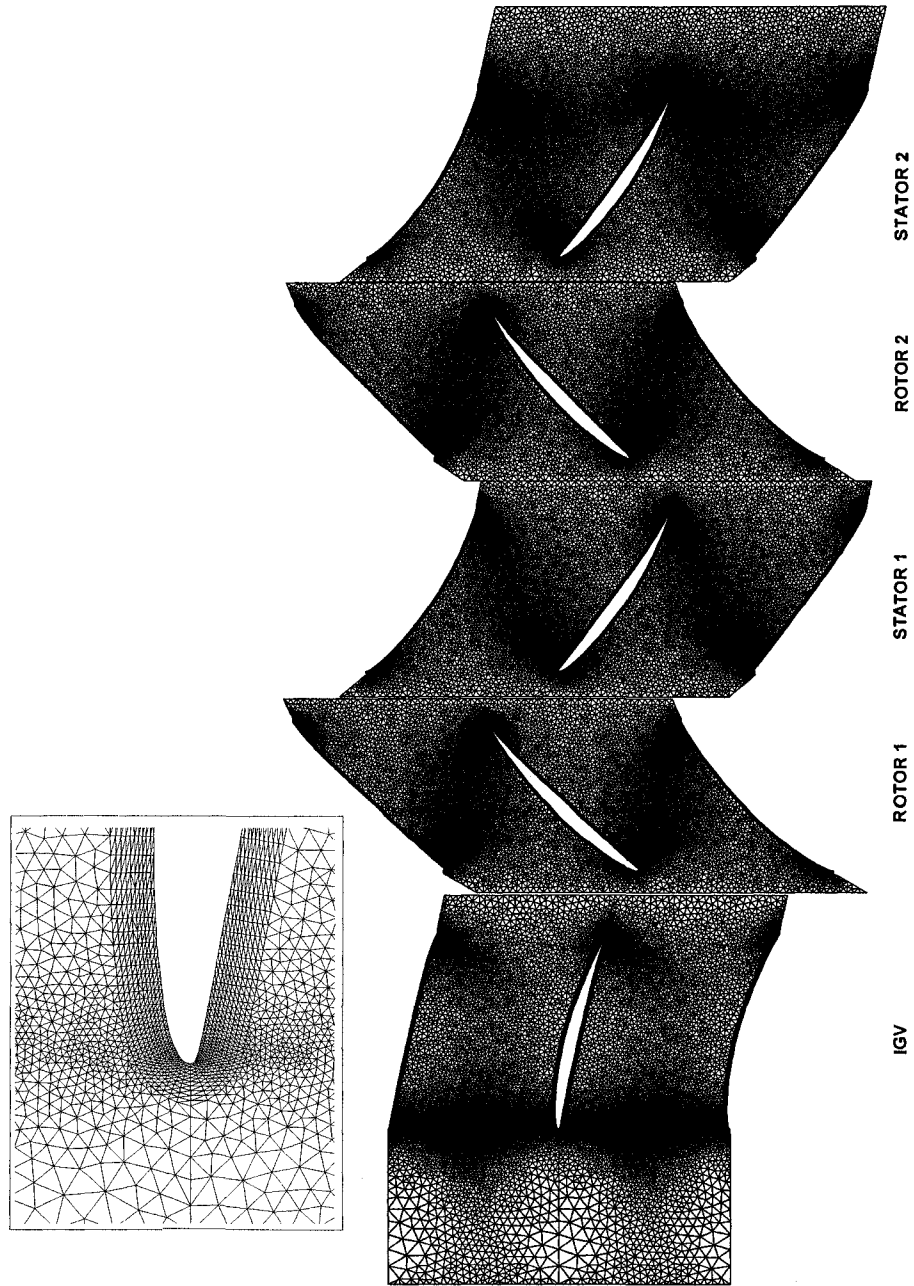
Abbildung 1.3: Hybrid mesh for a 2.5 multistage compressor

Chapter 2

Governing Equations and Numerical Implementation

After a short introduction of the governing flow equations, a thorough explanation on implementation of the quasi 3-D algorithm, steady mixing plane models and steady non-reflecting boundary conditions (NRBC) are presented in this chapter. Two different mixing plane models are presented as well as two different NRBC models. At the end a brief description on the numerical scheme of a multistage computation is given.

Mixing planes and NRBC are required to couple blade rows and bring the inflow and outflow boundaries relatively close to the regarding leading edge and trailing edge without affecting the flow field in the neighborhood of the blades. The implementation of quasi 3-D effects enables the flow simulation to take variations in stream tube thickness into account.

A validation on quasi 3-D and NRBC is given in Appendices A and B. Furthermore, a description of the general characteristics of the flow solver, i.e. governing equations, artificial dissipation, etc., is given in Appendix D.

2.1. Governing equations

The most complete description of compressible turbulent flow is by the Reynolds Averaged Navier-Stokes (RANS) equations. The equations are formulated in an absolute frame of reference but solved in a relative reference frame by applying an ALE formulation for domains with time-dependent boundaries. In the Cartesian frame the flux vectors are split up in inviscid components, i.e. F, and viscous components, i.e. G. The integral form of the RANS equations for an arbitrary control volume $\Omega(t)$ where n represents the outward unit vector of this control volume which is bounded by the surface $\Gamma(t)$, can be written in vector notation.

$$\frac{\partial}{\partial t} \iint_\Omega U \, d\Omega + \oint_{\partial\Omega} F \cdot n \, d\Gamma = \frac{1}{Re} \oint_{\partial\Omega} G \cdot n \, d\Gamma \tag{2.1}$$

Herein is

$$U = \begin{bmatrix} \rho \\ \rho w \\ \rho e \end{bmatrix}, \quad F = U\left(w - w_g\right) + \begin{bmatrix} 0 \\ p\delta_{ij} \\ w_j p \end{bmatrix}, \quad G = \begin{bmatrix} 0 \\ \tau_{ij} \\ w_k \tau_{ik} + \frac{\gamma}{\gamma-1}\left(\frac{\mu_l}{Pr_l} + \frac{\mu_t}{Pr_t}\right)\frac{\partial T}{\partial x_i} \end{bmatrix}. \tag{2.2}$$

Here, δ_{ij} represent the Kronecker delta function and $w - w_g$ is the velocity in the relative frame of reference. The viscous stress tensor τ_{ij} is expressed using the eddy viscosity concept which assumes that, in analogy with viscous stress in laminar flows, the turbulent stresses are proportional to mean velocity gradients:

$$\tau_{ij} = \mu\left(\frac{\partial w_i}{\partial x_j} + \frac{\partial w_j}{\partial x_i}\right) + \lambda\delta_{ij}(\nabla \cdot w) \tag{2.3}$$

where μ_l represents the molecular viscosity, μ_t denotes the turbulent eddy-viscosity, which must be determined by a suitable turbulence model. Therefore, $\mu = \mu_l + \mu_t$ is the total viscosity of the fluid. The value of λ is given by the Stokes relation

13

$\lambda = -\frac{2}{3}\mu$, while the laminar Prandtl number Pr_l is taken is 0.7 for air. The turbulent Prandtl number, Pr_t, is taken as 0.9. The turbulent viscosity is determined by the Baldwin-Lomax turbulence model [33] which is implemented due to its simplicity and success in simulating turbomachinery flow [39, 40]. In Appendix D a description of the turbulence model is given.

For an ideal gas, thermally and calorically, the pressure p and the total enthalpy h are related to density ρ, absolute velocity v and internal energy e

$$p = (\gamma - 1)\rho \left[e - \frac{|w|^2}{2} \right], \quad h = e + \frac{p}{\rho} \tag{2.4}$$

where γ is the constant specific heat ratio. All flow quantities are non-dimensionalized with total temperature and/or total pressure.

$$p = \frac{p}{p_0}, \quad T = \frac{T}{T_0}, \quad u, v = \frac{u, v}{\sqrt{RT_0}}, \quad \rho = \frac{\rho}{p_0/RT_0} \tag{2.5}$$

2.2. Quasi-three-dimensional-flow

There are many examples for applying quasi-3D Navier-Stokes equations in passage flow models [41, 42, 43]. In this work, 'quasi 3D' refers to the fact that the streamtube thickness varies in the axial direction. Moreover, no effort was made to implement centrifugal and Coriolis body forces into the governing equations. The stream tube thickness variation is considered to be the most important three dimensional effect at midspan in an axial turbomachine [23]. The nearly conservative form of the modified Navier-Stokes-Equations reads

$$h\frac{\partial U}{\partial t} + \nabla \cdot (h(F + G)) = \frac{dh}{dx}S \tag{2.6}$$

where h represents the stream tube thickness which is a known function in the x-direction and S denotes a source term in the form of

$$S = \begin{pmatrix} 0 \\ p - \frac{1}{Re}\tau_s \\ 0 \\ 0 \end{pmatrix}. \tag{2.7}$$

where τ_s are the stresses related to the source term. Equation 2.7 can be recast to separate the 2-D from the quasi-3-D terms [44].

$$\frac{\partial U}{\partial t} + \nabla \cdot (F + G) = \frac{1}{h}\frac{dh}{dx}(G - F - S) \tag{2.8}$$

The stream tube thickness variation has also to be taken into account for the stress term calculation in the viscous flux vector G, thus Eq. 2.3 is extended to:

$$\tau_{ii} = 2\mu\frac{\partial u}{\partial x} - \frac{2}{3}\mu\left(\frac{\partial u}{\partial x} + \frac{\partial v}{\partial y} + \frac{u}{h}\frac{dh}{dx}\right)$$

$$\tau_{ij} = \mu\left(\frac{\partial u}{\partial x} + \frac{\partial v}{\partial y}\right) \tag{2.9}$$

$$\tau_s = 2\mu\frac{u}{h}\frac{dh}{dx} - \frac{2}{3}\mu\left(\frac{\partial u}{\partial x} + \frac{\partial v}{\partial y} + \frac{u}{h}\frac{dh}{dx}\right)$$

$$\tag{2.10}$$

As a cell vertex finite volume scheme is used the discretized form of Eq. 2.6 can be written as a set of coupled ordinary differential equations:

$$\frac{d}{dt}(\Omega_i)\,U_i + \sum_e \left(\left(F_{x_e} - \frac{1}{Re}G_{x_e}\right)n_{x_e} + \left(F_{y_e} - \frac{1}{Re}G_{y_e}\right)n_{y_e}\right) = \frac{1}{h}\frac{dh}{dx}\left(\frac{1}{Re}G_i - F_i - S_i\right) \tag{2.11}$$

where the summation is taken over all edges of control volume i (with node i as its center), Ω_i is the control volume area, U_i is the solution vector, G_{x_e}, G_{y_e}, F_{x_e} and

F_{ye} are components of the flux vector on edge e, n_{xe}, n_{ye} are the components of the outward normal to edge e and G_i, F_i are the flux values at node i. The calculation of the fluxes on edge e amounts to a trapezoidal integration rule around the boundaries of the control surface and is second order accurate.

To determine the thickness of the stream surface, a first approximation is the blade height and its variation in the axial direction. More accurate stream tube thickness approximations are given in [45] where the endwall boundary layer is also taken into account. Appendix D presents the implementation of Eq. 2.11 in an explicit Runge-Kutta scheme. In Appendix A a validation case for inviscid flow is presented.

2.3. Mixing planes

Many averaging techniques have been introduced over the years [46, 27, 47] and were applied for 2D and 3D stage calculations. For a steady state interaction between adjacent blade rows a mixing plane is defined so as to communicate the flow properties which are associated with mass flow rate, momentum and energy fluxes. Instead of using an area- or mass averaged approach to obtain averaged values at the mixing plane the so-called „mixed out"-approach after Giles [24] is implemented. The reason therefore is the non-linear nature of the Euler equations so that common averaged values of flow properties cannot be calculated by using other averaged values. For example,

$$\bar{p} \neq (\gamma - 1)\bar{\rho}\left(\bar{e} - \frac{1}{2}\left(\bar{u}^2 + \bar{v}^2\right)\right) \tag{2.12}$$

A „mixed-out" flow field is the only rigorous definition [24] to perform an averaging procedure at inlet and outlet boundaries. The „mixed out" flow field approach starts

from the 2D Euler equations which are integrated in y-direction over the pitch, hence

$$\frac{d}{dx} \int_0^p F dy = \int_0^p \frac{\partial F}{\partial x} dy \qquad (2.13)$$

$$= \int_0^p -\frac{\partial G}{\partial x} dy$$

$$= G\left(0\right) - G\left(P\right)$$

$$= 0$$

This leads to the assumption that - if the flow field is uniform - the average flux $\overline{F}$ must be equal to a flux F which is based on uniform values of the primitive state vector U_F. Thus,

$$\rho_F u_F = \overline{F}_1$$

$$\rho_F u_F^2 + p_F = \overline{F}_2 \qquad (2.14)$$

$$\rho_F u_F v_F = \overline{F}_3$$

$$\rho_F u_F H_F = \overline{F}_4$$

Rearranging Eqs. 2.14 yields

$$p_F = \frac{1}{\gamma + 1} \left(\overline{F}_2 + \sqrt{\overline{F}_2^2 + (\gamma^2 - 1)\left(\overline{F}_2^2 + \overline{F}_3^2 - 2\overline{F}_1\overline{F}_4\right)} \right)$$

$$u_F = \frac{\overline{F}_2 - p_F}{\overline{F}_1}$$

$$v_F = \frac{\overline{F}_3}{\overline{F}_1} \qquad (2.15)$$

$$\rho_F = \frac{\overline{F}_1}{u_F}$$

This procedure gives rise to fictitious viscous losses at the outflow boundary and hence produces higher losses than other averaging techniques. The jump in pressure occurs downstream the mixing plane and during the iteration process the goal is to

match both sides of this interface. While the flux-averaged values at the outlet plane are calculated using the above mentioned method, at the corresponding inflow plane mass averaged values are applied. This method is valid due to the fact that the flux averaged quantities are compared *after* passing the mixing plane [25].

Another possibility to transfer the flow properties appropriately downstream is using the kinetic mixing approach [25]. While the mixed-out average assumes a uniform flow downstream, this approach is meant to represent the local state of the flow. As the kinetic energy average conserves mass and total enthalpy explicitly, the total pressure is not affected by mixing losses. Compared with Eq. 2.14 there is a fifth integrated property which is used to re-scale the averaged velocities: $\bar{u}_F^2 + \bar{v}_F^2 = \overline{V}^2$. The integrated properties are expressed by:

$$\rho_F u_F = \overline{F}_1$$

$$\rho_F u_F^2 = \overline{F}_2$$

$$\rho_F u_F v_F = \overline{F}_3 \qquad (2.16)$$

$$\rho_F u_F H_F = \overline{F}_4$$

$$\rho_F u_F V^2 = \overline{F}_5$$

That leads directly to the average properties, given by

$$\rho_F = \frac{\overline{F}_1}{u_F}$$

$$H_F = \frac{\overline{F}_4}{\overline{F}_1}$$

$$r_F = \sqrt{\frac{\overline{F}_5}{\overline{F}_1 \left(\overline{F}_2^2 + \overline{F}_3^2 \right)}} \qquad (2.17)$$

$$u_F = r_F \overline{F}_2$$

$$v_F = r_F \overline{F}_3$$

This mixing plane approach generally produces higher mass flow deviations than the „mixed out" counterpart [25].

2.4. Characteristic models in non-reflecting boundary conditions (NRBC)

Generally speaking, all subsonic boundaries are following the same principle: At inlet there are three incoming waves and one outgoing and at outlet there are three outgoing and one incoming wave. These waves are hereby referred to as characteristics. In this work Giles' [24] and Chima's [25] versions of non-reflecting boundaries are implemented. Both approaches have in common that they start from a linearized 1D Euler approach at the boundaries, given by

$$\frac{\partial U}{\partial t} + \mathbf{A}\frac{\partial U}{\partial x} = 0 \tag{2.18}$$

where U is the conservation variable vector (see Eq. 2.2) and $\mathbf{A}$ is

$$\mathbf{A} = \begin{pmatrix} u & \rho & 0 & 0 \\ 0 & u & 0 & \frac{1}{\rho} \\ 0 & 0 & u & 0 \\ 0 & \rho c^2 & 0 & u \end{pmatrix} \tag{2.19}$$

After several transformations we get (see [24]).

$$\frac{\partial \Phi}{\partial t} + \Lambda\frac{\partial \Phi}{\partial x} = 0 \tag{2.20}$$

19

where $\phi = \mathbf{K} \cdot U_p$ and

$$U_p = \begin{pmatrix} \rho \\ u \\ v \\ p \end{pmatrix} \qquad (2.21)$$

and with the general form of the changes in ϕ:

$$\delta\phi = \mathbf{K} \cdot \delta U_p \qquad (2.22)$$

Eqs. 2.22 and 2.21 are the basic equations of linearized, one-dimensional Euler boundary conditions. For non-reflecting boundary conditions the matrix $\mathbf{K}$ has the following form:

$$\mathbf{K} = \begin{pmatrix} -c^2 & 0 & 0 & 1 \\ 0 & 0 & \rho c & 0 \\ 0 & \rho c & 0 & 1 \\ 0 & -\rho c & 0 & 1 \end{pmatrix} \qquad (2.23)$$

By combining Eqs. 2.21 and 2.20 Λ can be rearranged to $\Lambda = \mathbf{K}^{-1}\mathbf{AK}$. The incorporation of the left and right Eigenvalues, $\mathbf{K}$ and $\mathbf{K}^{-1}$, is derived in [24] where the interested reader might explore the entire background of this theory. Equation 2.23 holds for steady/unsteady one-dimensional boundary conditions and - by incorporating slight modifications - for steady two dimensional boundary conditions. Equation 2.22 is the guiding term for calculations of flow properties at the inlet and outlet boundaries in this work.

2.5. 2-D NRBC

This approach refers to exact 2D steady boundary conditions and it basically requires two distinct treatments of characteristic variables. First, a 1D Euler environment is

created where the characteristic variables can be formulated as a perturbation of the flux averaged primitive variables at inlet or exit of a flow domain.

$$
\begin{pmatrix} \phi_1 \\ \phi_2 \\ \phi_3 \\ \phi_4 \end{pmatrix} = \begin{pmatrix} -c^2 & 0 & 0 & 1 \\ 0 & 0 & \rho c & 0 \\ 0 & \rho c & 0 & 1 \\ 0 & -\rho a & 0 & 1 \end{pmatrix} \begin{pmatrix} \rho - \bar{\rho} \\ u - \bar{u} \\ v - \bar{v} \\ p - \bar{p} \end{pmatrix} \tag{2.24}
$$

or

$$
\phi = \mathbf{K} \cdot \left(U_p - \bar{U}_p \right) \tag{2.25}
$$

Where the properties of matrix $\mathbf{K}$ refer to the flux averaged properties at the boundary. In this approach the results of Eq. 2.24 are required to compute the changes in characteristic variables. These changes $\delta\phi$ are of primary importance as they are used to calculate final primitive variables at the boundary and they are determined in a way such that outgoing waves are not reflected at the boundaries. Here, δU_p refers to the update of primitive variables at the boundaries.

$$
\delta U_p = \mathbf{K} \cdot \delta\phi \tag{2.26}
$$

The variable $\delta\phi$ of an incoming wave is composed of two parts. The first part refers to the average incoming characteristics which are specified in subsequent sections. The second part consists of local changes in incoming $\delta\phi$ specified by the non-reflecting boundary theory. The outgoing changes of characteristic variables are calculated by using the predicted changes in primitive flow variables at the boundary provided by the flow simulation of the internal flow field. The Jameson scheme, which is employed in this code, distributes properly the flow residuals of the primitive variables to the inlet and exit boundaries. Once all four $\delta\phi$ have been defined the changes of

21

characteristic variables can be converted back into changes of primitive variables.

$$\delta U_p = \mathbf{K}^{-1} \cdot \delta \phi \qquad (2.27)$$

For an inlet plane the changes in characteristic variables constitutes as

$$\begin{pmatrix} \delta\phi_1 \\ \delta\phi_2 \\ \delta\phi_3 \\ \delta\phi_4 \end{pmatrix} = \begin{pmatrix} \sigma\left(\delta\bar{\phi}_1 + \delta\phi_{1l}\right) \\ \sigma\left(\delta\bar{\phi}_2 + \delta\phi_{2l}\right) \\ \sigma\left(\delta\bar{\phi}_3 + \delta\phi_{3l}\right) \\ \delta\phi_{4,out} \end{pmatrix} \qquad (2.28)$$

and for an exit plane:

$$\begin{pmatrix} \delta\phi_1 \\ \delta\phi_2 \\ \delta\phi_3 \\ \delta\phi_4 \end{pmatrix} = \begin{pmatrix} \delta\phi_{1,out} \\ \delta\phi_{2,out} \\ \delta\phi_{3,out} \\ \sigma\left(\delta\bar{\phi}_4 + \delta\phi_{4l}\right) \end{pmatrix} \qquad (2.29)$$

An under relaxation factor σ is used to guarantee the wellposedness of the mathematical formulation. The ratio $\sigma = \frac{1}{N}$, where N is the number of boundary nodes, was found to work well. After substituting Eqs. 2.28/2.29 into Eq. 2.26 the updated primitive variables are calculated as

$$U_{p,new} = U_{p,old} + \delta U_p \qquad (2.30)$$

Subsonic exit

In cases where an adjacent blade row inlet boundary is communicating with an outlet boundary the average change (see Eq. 2.29) of the sole incoming change of the

characteristic variable $\delta\bar{\phi}_4$ can be written as

$$\delta\bar{\phi}_4 = \sigma\Delta\phi_4 \tag{2.31}$$

where $\Delta\phi_4$ is calculated from

$$
\begin{pmatrix} \Delta\phi_1 \\ \Delta\phi_2 \\ \Delta\phi_3 \\ \Delta\phi_4 \end{pmatrix}
=
\begin{pmatrix}
-a^2 & 0 & 0 & 1 \\
0 & 0 & \rho a & 0 \\
0 & \rho a & 0 & 1 \\
0 & -\rho a & 0 & 1
\end{pmatrix}
\begin{pmatrix}
\rho_{Fstator} - \rho_{Frotor} \\
u_{Fstator} - u_{Frotor} \\
v_{Fstator} - v_{Frotor} \\
p_{Fstator} - p_{Frotor}
\end{pmatrix}
\tag{2.32}
$$

According to Giles [24] the local changes of the fourth characteristic are determined as follows: the discrete Fourier transform of the characteristic variables two and three is calculated for a range of values of k from $-N/2 + 1$ to $+N/2 - 1$, where N is the number of equally spaced nodes at the boundary and j is the corresponding counter.

$$\delta\phi_{2,k} = \frac{1}{N}\sum_{j=1}^{N}\phi_{2,j}\exp\left(\frac{-i2\pi jk}{N}\right) \tag{2.33}$$

$$\delta\phi_{3,k} = \frac{1}{N}\sum_{j=1}^{N}\phi_{3,j}\exp\left(\frac{-i2\pi jk}{N}\right) \tag{2.34}$$

or in Cartesian form:

$$\delta\phi_{2,k} = \frac{1}{N}\sum_{j=1}^{N}\left(\phi_{2,j}\cos\left(\frac{2\pi jk}{N}\right) - i\sin\left(\frac{2\pi jk}{N}\right)\right) \tag{2.35}$$

$$\delta\phi_{3,k} = \frac{1}{N}\sum_{j=1}^{N}\left(\phi_{3,j}\cos\left(\frac{2\pi jk}{N}\right) - i\sin\left(\frac{2\pi jk}{N}\right)\right) \tag{2.36}$$

$\phi_{2,j}$ and $\phi_{3,j}$ refer to the node-wise characteristics based on Eq. 2.24 which are taken from extrapolation from the interior flow field. To get the desired local changes of the fourth characteristic variable, the next step is to calculate its steady state amplitude

for every single mode (e.g. k). This amplitude is given by a linear combination of the amplitudes of the second and third characteristics.

$$\delta\phi_{4,k} = \frac{2M_x}{\beta - M_y}\delta\phi_{2,k} - \frac{\beta + M_y}{\beta - M_y}\delta\phi_{3,k} \tag{2.37}$$

where

$$\beta = i\, sgn\,(k)\,\sqrt{1 - M^2} \tag{2.38}$$

To obtain the ideal non-reflecting steady-state values of the incoming fourth characteristic variable, the principle of complex conjugate pairs is used on the Fourier decomposition of the steady state amplitudes,

$$\delta\phi_{4,s,j} = 2Re\left\{\sum_{k=1}^{N/2-1}\left(\phi_{4,k}\left(\cos\left(\frac{2\pi jk}{N}\right) - i\sin\left(\frac{2\pi jk}{N}\right)\right)\right)\right\} \tag{2.39}$$

Eq. 2.39 is applied on every single exit boundary node. Finally, the local change of the fourth characteristic variable consists of the value of the fourth characteristic variable calculated in Eq. 2.24 and the value of the ideal non-reflecting steady state which was determined in Eq. 2.39.

$$\delta\phi_{4,local,j} = \phi_{4,s,j} - \phi_{4,j} \tag{2.40}$$

Thus,

$$\delta\phi_{4,j} = \sigma\left(\delta\bar{\phi}_4 - \delta\phi_{4,local,j}\right) \tag{2.41}$$

The result of Eq. 2.41 is inserted in Eq. 2.29 together with the predicted changes at the boundary from the residual calculation of the interior flow field. Once the flow simulation converged the values of $\delta\phi$ are driven to zero and steady conditions at the boundary are reached. In cases where no further blade row is following the average

part of $\delta\phi_4$ is calculated from a specified exit pressure instead of using Eq. 2.32,

$$\delta\bar{\phi}_4 = -2\left(p_F - p_{exit}\right) \tag{2.42}$$

where p_F is the average pressure extrapolated from the interior flow field.

Subsonic inlet

For inlet boundaries there are also two possible scenarios: The case where the flow has passed an upstream blade row is presented first. At rotor inlet for example, after the flow has passed the mixing plane, the average changes in incoming characteristic variables are (similar to Eq. 2.31):

$$\delta\bar{\phi}_1 = \sigma\Delta\phi_1 \tag{2.43}$$

$$\delta\bar{\phi}_2 = \sigma\Delta\phi_2 \tag{2.44}$$

$$\delta\bar{\phi}_3 = \sigma\Delta\phi_3 \tag{2.45}$$

The local changes of the characteristic variables are based on the amplitude of the outgoing fourth characteristic. Again, the number of modes k goes from $-N/2 + 1$ to $+N/2 - 1$.

$$\delta\phi_{2,k} = \frac{1}{N}\sum_{j=1}^{N}\phi_{2,j}\exp\left(\frac{-i2\pi jk}{N}\right) \tag{2.46}$$

In Cartesian form it reads:

$$\delta\phi_{4,k} = \frac{1}{N}\sum_{j=1}^{N}\left(\phi_{4,j}\cos\left(\frac{2\pi jk}{N}\right) - i\sin\left(\frac{2\pi jk}{N}\right)\right) \tag{2.47}$$

Similar to the subsonic exit, the correct steady state amplitude can be found by applying

$$\delta\phi_{2,k} = \frac{\beta + M_y}{1 + M_y}\delta\phi_{4,k} \tag{2.48}$$

The Transformation back into the physical domain gives the ideal non-reflecting steady state value.

$$\delta\phi_{2,s,j} = 2Re\left\{\sum_{k=1}^{N/2-1}\left(\phi_{2,k}\cos\left(\frac{2\pi jk}{N}\right) - i\sin\left(\frac{2\pi jk}{N}\right)\right)\right\} \qquad (2.49)$$

The ideal steady state changes of the local second characteristic are:

$$\delta\phi_{2,local,j} = \phi_{2,s,j} - \phi_{2,j} \qquad (2.50)$$

In order to obtain the local changes of the first and the third characteristic, we assume that perturbations from the average entropy and enthalpy are providing the necessary local residuals.

$$R_{1,j} = p\left(S_j - \bar{S}\right) \qquad (2.51)$$

$$R_{3,j} = p\left(H_j - \bar{H}\right) \qquad (2.52)$$

To convert these residuals into local characteristic changes the Newton-Raphson method is applied:

$$\begin{pmatrix} R_{1,j} \\ R_{2,j} \end{pmatrix}^n = \begin{pmatrix} 1 & 0 & 0 \\ \frac{1}{\gamma-1} & M_y & \frac{1}{2}\left(1+M_x\right) \end{pmatrix} \begin{pmatrix} \delta\phi_{1,local,j} \\ \delta\phi_{2,local,j} \\ \delta\phi_{3,local,j} \end{pmatrix} \qquad (2.53)$$

Hence, the solution is

$$\delta\phi_{1,local,j} = -R_{1,j}$$

$$\delta\phi_{3,local,j} = -\frac{2}{1+M_x}\left(\frac{1}{\gamma-1}\delta\phi_{1,s,j} + M_y\delta\phi_{2,s,j} + R_{3,j}\right) \qquad (2.54)$$

26

Equation 2.54 gives the local changes of the first and third characteristics and combined with the average global changes from Eq. 2.43, we get the final necessary modifications.

$$\delta\phi_{1,j} = \sigma\left(\delta\bar{\phi}_1 - \delta\phi_{1,local,j}\right) \tag{2.55}$$

$$\delta\phi_{2,j} = \sigma\left(\delta\bar{\phi}_2 - \delta\phi_{2,local,j}\right) \tag{2.56}$$

$$\delta\phi_{3,j} = \sigma\left(\delta\bar{\phi}_3 - \delta\phi_{3,local,j}\right) \tag{2.57}$$

The outgoing fourth characteristic is calculated by using Eq. 2.22 and the distributed flow residuals coming from the interior flow calculation. The next case refers to a subsonic inflow boundary with no adjacent upstream blade row. There, the average changes of incoming characteristic variables are calculated based on the assumption that average entropy, flow angle a stagnation enthalpy are specified. In the present case the entropy and total enthalpy were set to zero which corresponds to the non-dimensionalization given in Eq. 2.5. The inlet flow angle is specified per-se. The resulting local residuals at the inlet boundary are expressed as:

$$
\begin{aligned}
R_1 &= p\bar{S} \\
R_2 &= \rho c\left(v_F - \tan\left(\alpha_{inl}\right)u_F\right) \\
R_3 &= \rho\left(\bar{H} - \frac{\gamma}{\gamma-1}\right)
\end{aligned}
\tag{2.58}
$$

By applying a Newton-Raphson procedure the average changes of the incoming characteristic variables can be written as

$$\begin{pmatrix} R_1 \\ R_2 \\ R_3 \end{pmatrix}^n + \frac{\partial\left(R_1, R_2, R_3\right)}{\partial\left(c_1, c_2, c_3\right)}\begin{pmatrix} \delta\bar{\phi}_1 \\ \delta\bar{\phi}_2 \\ \delta\bar{\phi}_3 \end{pmatrix} = 0 \tag{2.59}$$

After some tedious math these average changes are expressed as

$$
\begin{pmatrix} \delta\bar{\phi}_1 \\ \delta\bar{\phi}_2 \\ \delta\bar{\phi}_3 \end{pmatrix} = \frac{-1}{1 + M_x + M_y \tan{(\alpha_{inl})}} \begin{pmatrix} 1 + M_x + M_y \tan{(\alpha_{inl})} & 0 & 0 \\ -\frac{1}{\gamma-1} \tan{(\alpha_{inl})} & 1 + M_x & \tan{(\alpha_{inl})} \\ \frac{2}{\gamma-1} & -2M_y & 2 \end{pmatrix} \begin{pmatrix} R_1 \\ R_2 \\ R_3 \end{pmatrix}
\tag{2.60}
$$

The result of Eq. 2.60 can be inserted into Eq. 2.28 which leads to the final changes of incoming characteristic variables.

2.6.   1-D NRBC

The approach of Chima [25], who is also referring to Giles non-reflecting approach, is comparatively simple as it is based on one-dimensional unsteady boundary conditions only. In this approach there is no need for local characteristic changes as the updated primitive variables are directly extracted from Eq. 2.24. The corresponding characteristic variables can be regarded as local deviations from a specified average value. In this approach these average values as well as the elements of matrix $\mathbf{K}$ are taken from the mixing plane of the adjacent blade row exit or inlet. At inlet the first three incoming characteristics are set to zero and at outlet the fourth characteristic is set to zero.

Subsonic inlet

At a subsonic rotor inlet boundary for example the corresponding primitive variables can be calculated by respecting the fact that the first three characteristics are set to

zero and the fourth, $\phi_{4,ex}$, is extrapolated from the interior flow field.

$$\rho = \rho_{F,stator} + \frac{\phi_{4,ex}}{2c^2_{F,stator}}$$

$$u = u_{F,stator} + \frac{\phi_{4,ex}}{2}\left(\rho c\right)_{F,stator} \qquad (2.61)$$

$$v = v_{F,stator}$$

$$p = p_{F,stator} + \frac{\phi_{4,ex}}{2},$$

where

$$\phi_{4,ex,} = -\left(\rho c\right)_{F,stator}\left(u_{ex} - u_{F,stator}\right) + \left(p_{ex} - p_{F,stator}\right). \qquad (2.62)$$

Density, pressure and axial velocity are dependent on the fourth characteristic variable while the local circumferential velocity at inlet is assumed to be constant over the pitch. Equation 2.61 directly presents the üpdatedprimitive variables at the boundary.

Subsonic exit

At the exit of a blade row, e.g. stator, the fourth characteristic variable is supposed to be zero and the other three are extrapolated from the upstream flow field. This leads to:

$$\rho = \rho_{F,rotor} + \frac{-\phi_{1,ex} + \phi_{2,ex}/2}{2c^2_{F,rotor}}$$

$$u = u_{F,rotor} + \frac{\phi_{2,ex}}{2\left(\rho c\right)_{F,rotor}} \qquad (2.63)$$

$$v = v_{F,rotor}$$

$$p = p_{F,rotor} + \frac{\phi_{2,ex} + \phi_{4,ex}}{2},$$

where

$$\phi_{1,ex,} = c^2_{F,rotor}\left(\rho_{ex} - \rho_{F,rotor}\right) + \left(p_{ex} - p_{F,rotor}\right). \qquad (2.64)$$

and

$$\phi_{2,ex,} = \left(\rho c^2\right)_{F,rotor} \left(u_{ex} - u_{F,rotor}\right) + \left(p_{ex} - p_{F,rotor}\right). \tag{2.65}$$

Substituting Eq. 2.65 into the pressure term of Eq 2.63 gives:

$$p = \frac{1}{2}\left[p_{F,stator} + p_e x + \left(\rho c^2\right)_{F,rotor}\left(u_{ex} - u_{F,rotor}\right)\right] \tag{2.66}$$

In order to reduce pressure disturbances at the boundary caused by entropy non-uniformities, Chima proposes a small modification in Eq. 2.66 by replacing the convective speed $c_{F,stator}$ with $|u|_{F,stator}$. Thus,

$$p = \frac{1}{2}\left[p_{F,stator} + p_e x + \left(\rho |u|_{F,stator}\right)_{F,rotor}\left(u_{ex} - u_{F,rotor}\right)\right] \tag{2.67}$$

2.7. Comments on NRBC-models

NRBC based on characteristic methods present the common way to model exit and inlet boundaries in multistage turbomachinery flow simulation [26, 16, 48]. Combined with a mixing plane using flux-averaged primitive variables it is supposed to provide satisfactory results. Giles already stated in his article [24] that his solution holds for specific exit flow conditions only, namely flows with uniform exit entropies. Chima's modification (see Eq. 2.67) was supposed to suppress pressure disturbances caused by entropy non-uniformities at the exit boundaries, however, its success highly depends on the choice of the flow solver [49]. The application of these modified 1D Euler equations in the present code [20, 50] caused a local non-physical pressure source near the exit boundary. Furthermore, the deviation of mass flow at the mixing plane between any two adjacent blade regions is increasing substantially.

Giles' approach is suitable for calculations where a rapid convergence of the flow solution is a secondary objective. Due to the under relaxation factor (see Eqs.

2.28, 2.29) the update at the inflow and outflow boundaries is delayed and especially in multistage inverse design a rapid match of flow conditions at inlet and adjacent outlet boundary is essential. For a single stage Giles' approach gives satisfying results. Inverse design of a multistage turbomachine, e.g., in a 2.5 stage, requires a fast mean of communication between adjacent blade rows; this was resolved by using Chima's approach. In Appendix B Giles' and Chima's approaches are compared and analyzed for viscous and inviscid flow cases and the result showed that Giles' approach gives slightly better results than Chima's approach for both inviscid and viscous flows.

2.8.   Numerical scheme for multistage calculation

The numerical scheme of five blade rows required an efficient organization of pre-processing, flow simulation and post processing modules in order to decrease the computational time of a multistage simulation. The basic code is organized in a way such that parallel computation can easily be applied to the present scheme. Figure 2.1 presents the main blocks of the program. First, the mesh and initial conditions are set up for every blade region before running the RANS solver. The flow information at each mixing plane is exchanged after every pseudo-time step. This was considered to be frequent enough for a rapid overall convergence. Details on the flow solver are given in Appendix D. The inverse mode is executed after all blade rows have reached a required convergence level. In Chapter 3 the inverse algorithm is described more thoroughly. This algorithm was found to be efficient and modular so that it can be easily parallelized in the future.
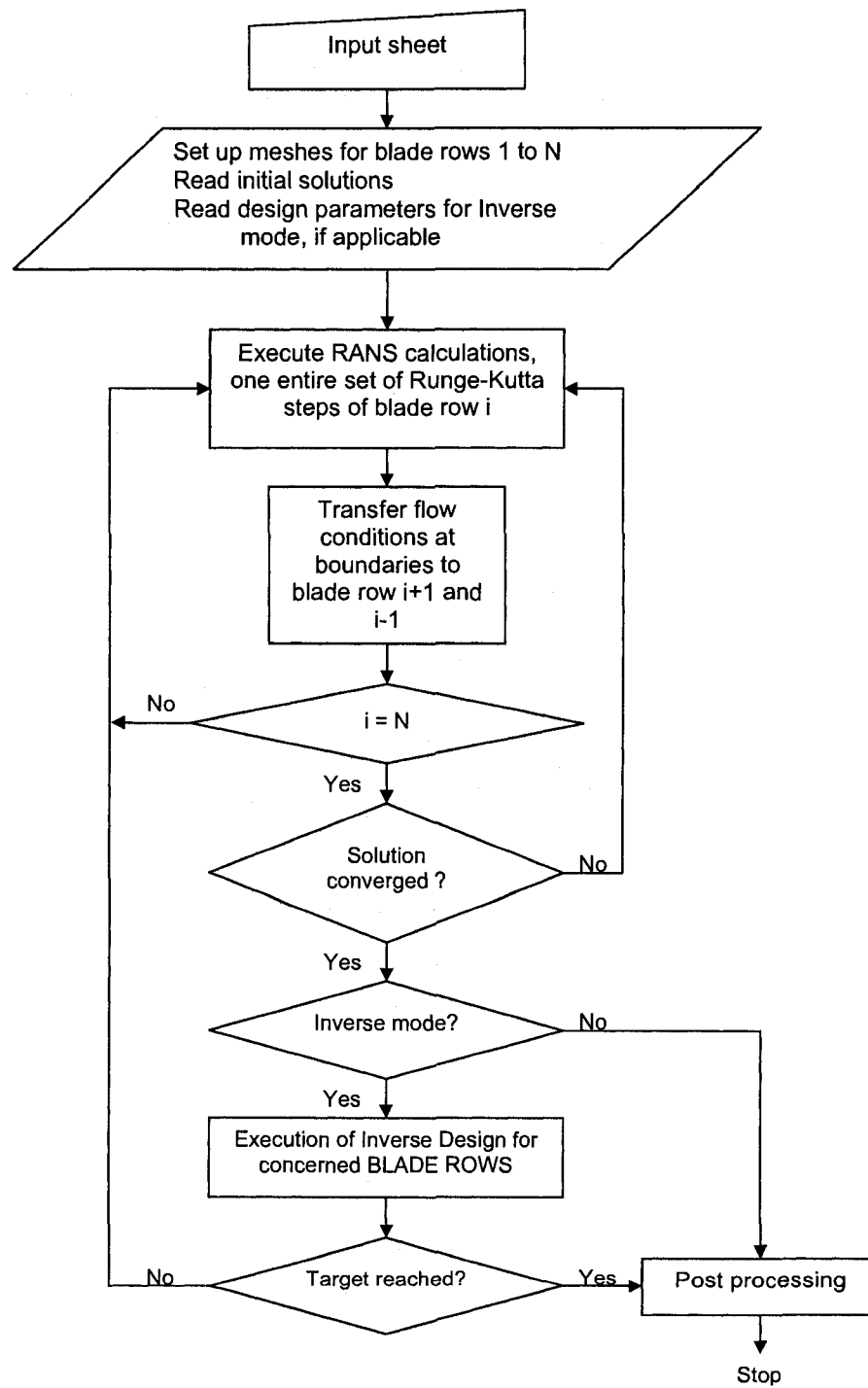
Abbildung 2.1: Numerical scheme for multistage calculation

Chapter 3

Inverse Design Methodology

In this chapter, the inverse design methodology is presented and is validated for two different turbine stages. The basic idea is that, as long as the pressure distribution on the blade surfaces is different from the target distribution, the blade will move with a virtual velocity that is proportional to the difference between the current and the target pressure distribution. It follows that the virtual velocity will tend to zero as the pressure approaches. This virtual blade velocity is derived from the difference in momentum fluxes between the current and the target ones on the blade surfaces; this velocity drives the blade shape to the one that would produce the target, e.g. loading, while the RANS equations are solved in a time accurate fashion. The governing equations which are solved in Arbitrary Lagrangian-Eulerian (ALE) form update the flow field by taking the movement and deformation of the computational grid into account. The design process requires first a specified target performance on each blade surface. In a multistage environment the target is most often connected to a pressure loading. A hypothetic subsonic single stage turbine and the E/TU-3 turbine stage are used to validate the inverse method and to demonstrate the flexibility and robustness of the methodology.

3.1. Inverse design formulation

The blade motion, which basically describes a wall movement approach, is derived from the difference between the actual and target performance on the blade suction and pressure sides. A balance of transient momentum flux $\mathbf{F}$ and design momentum flux $\mathbf{F^d}$ results in a virtual velocity distribution $\mathbf{v} = (u^v, v^v)$ which is applied on the blade suction and pressure surfaces. When the blade is moving with a virtual velocity the momentum flux in the Navier-Stokes equations takes the form:

$$\mathbf{F} = \left[\begin{array}{c} (\rho u^v u^v + p)\, n_x + (\rho u^v v^v)\, n_y \\ (\rho u^v v^v)\, n_x + (\rho v^v v^v + p)\, n_y \end{array} \right] \tag{3.1}$$

where the vector normal to the blade surfaces is $\mathbf{n} = (n_x, n_y)$. The initial blade geometry will be modified according to Eq. 3.1 and eventually it will reach a shape that would satisfy the target pressure. Once the target condition is reached, the virtual velocities vanish and the design momentum flux reads:

$$\mathbf{F^d} = \left[\begin{array}{c} (p^d n_x) \\ (p^d n_y) \end{array} \right] \tag{3.2}$$

By equating the two momentum fluxes $\mathbf{F}$ and $\mathbf{F^d}$, given in Eq. 3.1 and Eq. 3.2, the virtual velocity components in x- and y- directions are obtained:

$$\begin{aligned} v^v &= \pm \left(\frac{n_y^2}{n_x^2 + n_y^2} \frac{|p^d - p|}{\rho} \right)^{\frac{1}{2}} \\ u^v &= v^v \frac{n_x}{n_y} \end{aligned} \tag{3.3}$$

A positive difference between target and actual pressure on the suction side induces a positive virtual velocity and vice versa on the pressure side. For convenience the

normal velocity vector to the wall is used and it is calculated from:

$$v_n^v = \mathbf{v}^v \cdot \mathbf{n} \qquad (3.4)$$

The corresponding wall displacement δs is proportional to v_n^v, however, it points in the opposite direction to fulfill the no-penetration condition on the wall. Hence,

$$\delta s = -\omega \, v_n^v \, \delta t \qquad (3.5)$$

where δt is the user defined physical time step of the calculation, and ω is introduced as a relaxation factor. The negative sign in Eq. 3.5 indicates that the wall moves in a direction opposite to v_n^v.

A stability analysis of the scheme shows that the virtual velocity distribution must be heavily under-relaxed to ensure convergence of the scheme to a steady state solution [5]. The relaxation factor is found to have the following form:

$$\omega = \varepsilon \cdot (1/c)\sqrt{|\Delta p|/\rho} \qquad (3.6)$$

where c is the speed of sound and ε is a constant. The suggested value of ε was 0.01-0.02 [18], however the present implementation allows for higher values of ε, namely $\varepsilon = 0.2$ or 0.1 for subsonic or transonic outflow design cases.

The presented formulation works well for inviscid and viscous flows although in Eq. 3.1 the viscous terms were neglected and the balance of convective terms only was used to move the walls towards a shape which satisfies a target pressure distribution [51].

3.2. Inverse design variables

The differences in design philosophy between a multistage and a single blade row are substantial [16]. In a single blade row redesign case the designer ordinarily handles prescribed boundary conditions such as fixed inlet flow angles and inlet Mach number. Having these constraints in mind the designer can choose between imposing a target pressure loading and thickness distribution or pressure distribution on the blade surfaces. In a stage case the inlet flow conditions after the first blade row might vary due to various reasons and it directly affects the pressure distribution of the blade row which is inversely designed. If the pressure level drops or rises, due to a transient variation of pressure loading for example, an imposed absolute target pressure distribution can no longer be matched. On this account it is more convenient in a multistage environment to define a target blade loading, i.e. the pressure difference between the blade suction and pressure side. To a designer it might be also important to prescribe the blade thickness distribution as structural and manufacturing conditions are already defined.

For a single stage it is possible to design for a target pressure distribution as the mentioned transient pressure variations are ordinarily small. When the pressure distribution is prescribed on the blade pressure side and suction side, the blade displacement is directly found by solving Eqs. 3.1-3.6.

In case of a prescribed loading distribution as the design input, the corresponding surface pressure distributions need to be computed, because the numerical implementation requires these pressures to compute the virtual wall velocity in Eq. 3.1. The required pressure distributions can be derived from the prescribed target loading distribution as follows:

$$p_d^{\pm} = \frac{1}{2}[(p^+ + p^-) \pm \Delta p_d] \tag{3.7}$$

where p^+ and p^- are the calculated blade suction and pressure side pressures. In some

cases, Eq. 3.7 may result in a non-physical value for p_d^+ namely, $p_d^+ > 1$ during the convergence process. Usually, the pressure distribution on the pressure side is less sensitive to modifications in geometry, so for such cases, p_d^+ is taken to be the current value computed from the flow field:

$$p_d^+ = p^+ \quad and \quad p_d^- = p_d^+ - \Delta p_d \tag{3.8}$$

Note that p^+ will change with the iterations since the tangential thickness is fixed.

To satisfy the imposed blade thickness, the new blade shape is generated as follows. The camberline $f(x)$ is displaced by the average change in blade shape on both blade surfaces which are obtained from Eq. 3.5. The imposed blade thickness is then applied to this new camberline in order to generate new suction and pressure side profiles.

$$f(x)_{new} = f(x)_{old} \pm 0.5(\delta s^+ + \delta s^-) \tag{3.9}$$

$$y(x)_{new}^{\pm} = f(x)_{new} \pm 0.5T(x) \tag{3.10}$$

In case of multistage application, the resulting blade geometry is scaled to maintain the initially defined chord length which is not necessarily equal to one. The grid points are brought back to their initial x-location which leads to a blade movement in y-direction only. To ensure a smooth blade profile, the blade camberline $f(x)_{new}$ is smoothed before generating the blade profiles, $y(x)_{new}^{\pm}$, by applying the following formulation:

$$f_j = f_j + \omega_s[|f_{j+1} - f_j|(f_{j+1} - f_j) + |f_{j-1} - f_j|(f_{j-1} - f_j)] \tag{3.11}$$

where j refers to discrete points on the blade camberline. A typical value for the smoothing coefficient is $\omega_s = 0.2$. This smoothing is supposed to eliminate small non-physical geometry oscillations that can appear in the final blade shape. However, the

correct blade camberline for an arbitrary prescribed loading may not be genuinely smooth and the application of Eq. 3.11 may introduce a real position error. Therefore it is necessary to find the correct balance between a smooth blade profile and a well matched target pressure distribution.

3.3. Inverse design algorithm

The design technique described in the previous section was implemented into the unsteady RANS equations where the blade movement is the source of unsteadiness. Another source is the upstream and downstream traveling pressure wave which originates from the back pressure adjustment. After each geometry modification step, a time-accurate solution is obtained for the flow fields in every single blade row region. As mentioned in Chapter 1, the time accurate formulation eliminates the temporal errors and hence it improves the scheme robustness.

Figure 3.1 shows the inverse design algorithm in detail. Starting from a semi-converged solution on a trial geometry and prescribed target loading or pressure distributions (Eq. 3.7), the difference between actual and target pressure distribution is used to compute a virtual velocity distributions from Eq. 3.3 for the blade surfaces from which the local geometry modifications are deduced. After the geometry modifications, the computational mesh is adjusted using trans-finite interpolation. The grid displacements and hence the grid velocities are then computed for the entire computational domain of the corresponding blade row using the space conservation law [37]. The unsteady governing equations are marched in pseudo-time to converge the local problem and obtain the transient pressure distribution on the modified geometry. The overall computational time for an inverse calculation depends on the number of geometry modifications, the computing time required to obtain the time accurate solution after each geometry modification and the number of parallel simulated blade

```
         ┌─────────────────────────────────────────┐
         │   Initial Geometry, Target quantities   │
         └─────────────────────────────────────────┘
                            │
                            ▼
         ┌─────────────────────────────────────────┐
    ┌───▶│       Time-accurate 2D RANS             │
    │    │            Calculation                  │
    │    └─────────────────────────────────────────┘
    │                       │
    │                       ▼
    │    ┌─────────────────────────────────────────┐
    │    │   Transfer boundary conditions to       │
    │    │        adjacent blade rows              │
    │    └─────────────────────────────────────────┘
    │                       │
    │                       ▼
    │                   ╱ Calculated ╲     Yes
    │                  ⟨  = Target     ⟩──────────▶  Stop
    │                   ╲             ╱
    │                       │ no
    │                       ▼
    │    ┌─────────────────────────────────────────┐
    │    │     Compute Virtual Wall Velocities     │
    │    └─────────────────────────────────────────┘
    │                       │
    │                       ▼
    │    ┌─────────────────────────────────────────┐
    │    │         Modify Blade Geometry           │
    │    └─────────────────────────────────────────┘
    │                       │
    │                       ▼
    │    ┌─────────────────────────────────────────┐
    │    │      Adjust Computational Mesh          │
    │    └─────────────────────────────────────────┘
    │                       │
    │                       ▼
    │    ┌─────────────────────────────────────────┐
    │    │     Compute Grid Velocities (SCL)       │
    │    └─────────────────────────────────────────┘
    │                       │
    │                       ▼
    │    ┌─────────────────────────────────────────┐
    │    │   Update inlet and outlet boundary      │
    │    │            conditions                   │
    │    └─────────────────────────────────────────┘
    │                       │
    └───────────────────────┘
```
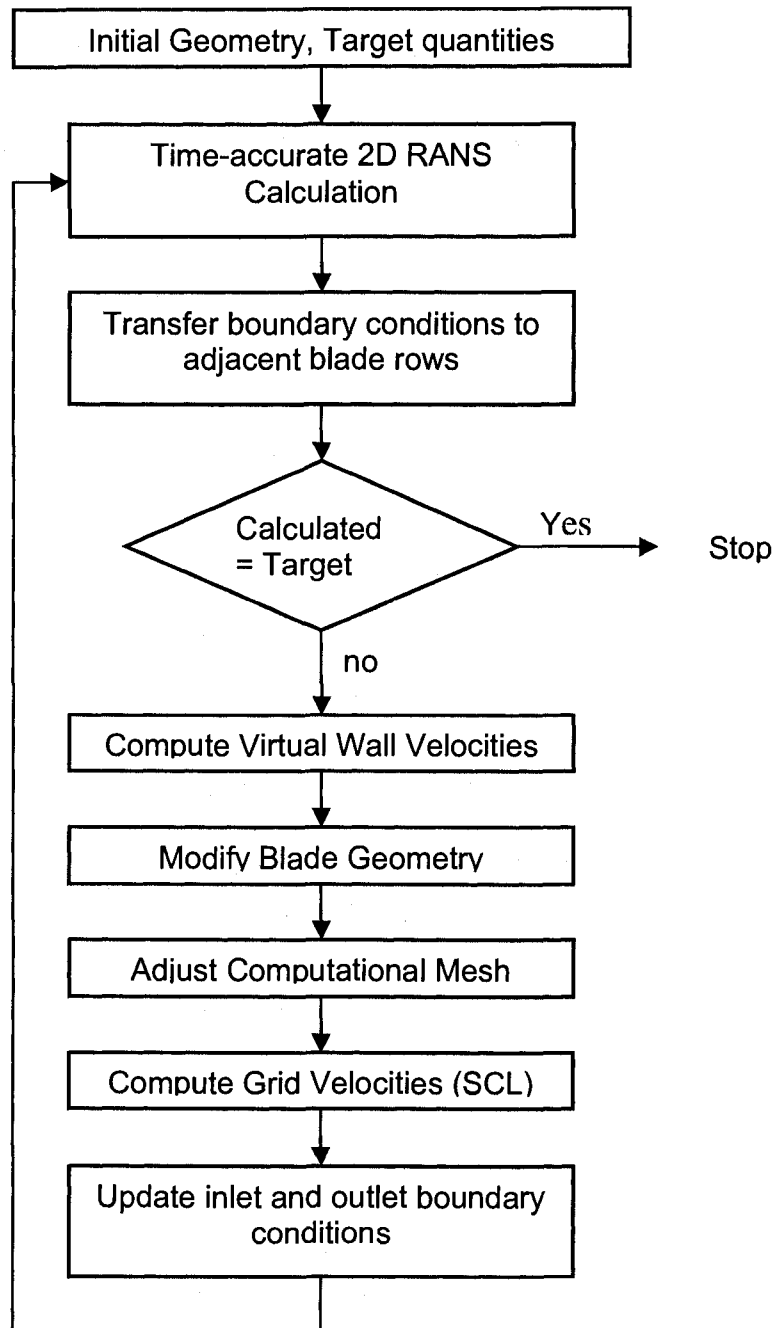
Abbildung 3.1: Computation algorithm for multistage inverse design

rows. The process is repeated until the L_2 norm of the grid velocities is decreased to the desired tolerance, which ensures that a steady state condition is reached, where the virtual velocity is asymptotically vanishing and the target pressure distribution is achieved on the latest blade profile.

3.4. Design considerations

Detailed blade shapes are obtained towards the end of a compressor or turbine design cycle. The blade shapes must satisfy several geometric and non-geometric constraints. Typically the blade chord, number of blades, inlet flow angle at the first blade row, mass flow rate, degree of stage reaction, rotational speed, limits of incidence angles and desired static and total pressure ratios will be specified before the aerodynamic design process starts. In addition, geometric constraints may exist e.g. maximum or minimum blade thickness or prescribed leading and trailing edge radii should be closely matched.

The present inverse technique allows for some of these constraints to be readily satisfied. Most non-geometric constraints are directly satisfied through the selection of inflow and outflow boundary conditions. Basic blade geometric constraints are defined by the conditions given above as well as preliminary considerations of stage matching. Specific geometric constraints e.g. LE/TE shapes can be obtained by imposing a specific geometry in the blade LE/TE regions, which usually extend between 1% and 3% chord, and running the code in analysis mode in these two regions. To ensure the profile smoothness at the transition from design mode to analysis mode, the slope of the camberline and the blade thickness in the analysis regions are matched with that prevailing in the design region; thus ensuring that the blade LE/TE shapes are closely controlled and that the blade shape is also closed [20].

3.5. Inverse design validation

This section presents the validation of the inverse method when applied on two subsonic single stage cases. In the first case the initial and modified stator and rotor geometries are hypothetical. The validation is focused on recovering of the original rotor geometry starting from a modified rotor blade shape, and the original blade pressure distribution as target. The second case deals with the recovery of the original stator geometry of the E/TU-3 single stage turbine [52]. If the inverse method is valid in a stage environment, it should recover the original blade rows geometry and match the prescribed pressures.

3.5.1 Hypothetical single turbine stage

The geometrical parameters of this stage are condensed in Tab. 3.1 and the initial flow conditions are presented in Tab. 3.2. At design point the maximum Mach number along the stator is close to 0.6 while the maximum flow Mach number at the original rotor does not exceed 0.85. The stage reaction is on the high side namely 0.8. The modified rotor shows a similar maximum flow Mach number of 0.85 but it stretches across 30% chord. The error in mass flow rate at the mixing plane was 0.04% which is very low. For the original and the modified rotor cases the flow is subsonic throughout and is well behaved. Figure 3.2 shows the stage set up and isentropic Mach number contours.

The stage was first analyzed and the pressure distribution that was obtained on the rotor surfaces was used as input to the inverse design mode but starting from a modified rotor geometry. In other words, the Navier-Stokes program was run in inverse mode in the rotor region while it was run in analysis mode in the stator region. Starting from a rotor geometry which has a 10% higher maximum thickness than the target, the imposed pressure distributions p^+ and p^- are supposed to guide

the blade shape towards the original one. Figure 3.5 shows initial, target and design isentropic Mach number which corresponds to the pressure distribution of the rotor blade row.

The target pressure distribution was achieved relatively fast after 150 design steps and the L_2-norm of the displacements went down to 10^{-4} which indicated that the target pressure distribution was achieved. At each time step, the geometry is modified and solution of the local problem is obtained after 50 Runge-Kutta iterations in pseudo-time. The inlet flow angle at rotor changed by 0.03°, and the mass flow rate differed by 0.08% compared to the original one. Figure 3.4 presents the initial, target and design rotor geometry where it can be seen that the target shape was obtained. The achieved design showed a good agreement to the original stage results.

Figure 3.6 shows the blade shape of a validation case where the design process was not solved in a time-accurate fashion but as a steady state problem. Hence, the mesh movement was not taken into account and Ghaly and Daneshkhah [19] demonstrated that such a quasi-steady formulation may fail to converge or at least spoil the solution. The reason therefore is that errors resulting from a quasi-steady solution are propagating into the blade shape which in turn is affecting the pressure distribution at the next iteration step. It can be depicted that the original blade shape was not exactly recovered but slightly and constantly displaced towards the trailing edge. The major shape modifications were executed at 25% chord and there the deviation from the original shape starts. This fact confirms once more the conclusion reached by Ghaly and Daneshkhah [19] concerning the necessity of computing a time-accurate solution when inverse designing a blade.

3.5.2   E/TU-3 single turbine stage

The second case validates the inverse approach by recovering the stator of the E/TU-3 turbine stage. The results of the stage analysis is summarized in Appendix C, where

the CFD-multistage code is assessed on this E/TU-3 turbine stage. The pressure distributions of the original stator were used as input to the inverse design mode but starting from a modified stator geometry. Figure 3.9 shows the initial guess of the stator profile, the target profile and the inversely designed profile, where the last two profiles are almost identical. The target and the inversely calculated pressure distributions, presented in Fig. 3.10, indicate a rather excellent agreement. The flow characteristics of the target and inversely designed stator blades are summarized in Table 3.3, which shows an acceptable difference in the reduced mass flow rate of 0.23% and in inlet flow angle of 0.2°. (To obtain a unique blade shape, the mass flow rate has to be specified [21]; that was accomplished by varying the back pressure downstream of the rotor.)

The target stator profile was well recovered and the target pressure distribution was achieved rather accurately, see Figs. 3.9 and 3.10. Due to this fact, the stage calculation produced the expected performance when the inverse design process had converged. It took about 450 time steps (each involving a geometry modification) to recover the original stator profile and to obtain the target stage performance. A time accurate solution of the local problem was achieved after 200 iterations after each geometry modification which represents a 25% increase compared to the single blade row inverse design method [19] because of the unsteady interaction between the stator and rotor regions. The aerodynamic characteristics of the original profile, the inversely computed profile and the one used as initial guess for the inverse design calculation, are listed in Tab. 3.3, which shows that the original and the inversely computed profiles are in good agreement.

Tabelle 3.1: Hypothetical single stage geometric characteristics

	Stator	Rotor
β_1	25°	30°
β_2	55°	57°
Pitch to chord ratio	1.74	1.62
Axial gap to stator chord	0.10	0.10

Tabelle 3.2: Summary of design validation for the hypothetical stage

	Initial	Target	Design	Error
$\alpha_{2,rotor}$	-60.4 °	-59.9°	-59.9 °	0.0°
$\dot{m}_{rotor}$	0.2525	0.2503	0.2501	0.08%
ζ_{rotor}	15.8%	12.9%	12.93%	0.03%

Tabelle 3.3: Summary of design validation of E/TU-3 stage

	Initial	Target	Design	Error
$\alpha_{2,stator}$	-66.2°	-67.9°	-67.7°	0.2°
$\dot{m}_{stator}$	0.2061	0.2120	0.2115	0.23%
ζ_{stator}	6.82%	6.10%	6.11%	0.20%
η_{is}	89.2%	89.7%	89.8%	0.11%
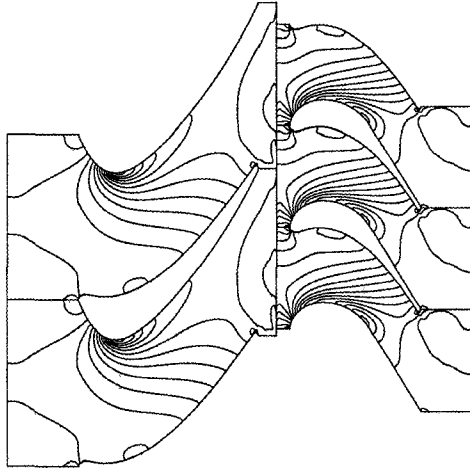
Abbildung 3.2: Isentropic Mach contour lines for the original stage
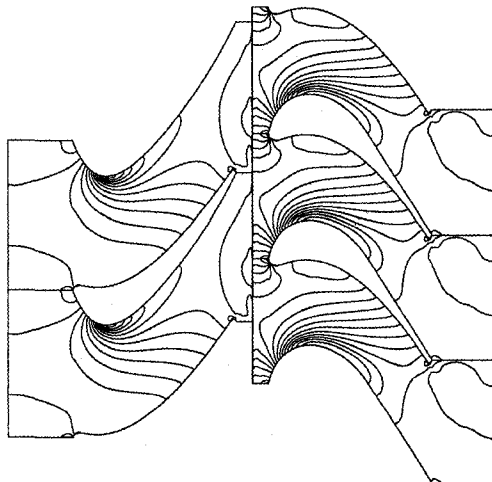
Abbildung 3.3: Isentropic Mach contour lines for the modified stage
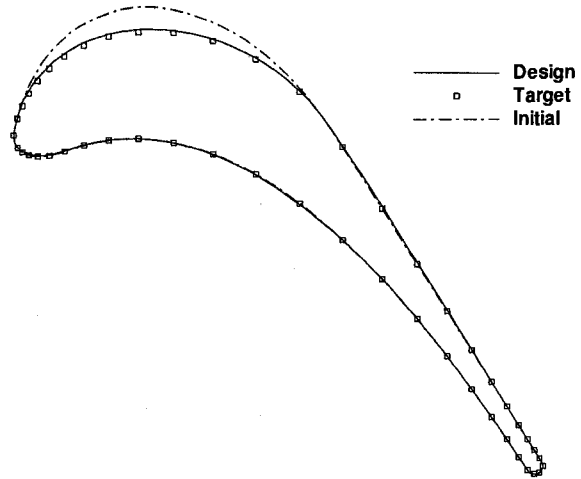
Abbildung 3.4: Initial, target and design rotor geometry
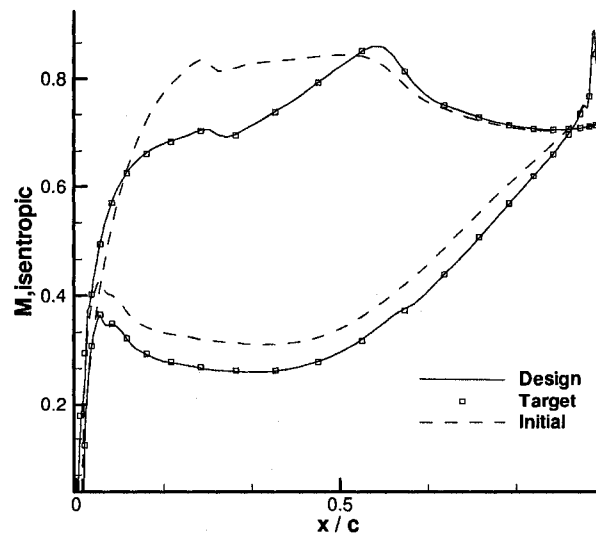
Abbildung 3.5: Initial, target and design rotor isentropic Mach number distribution
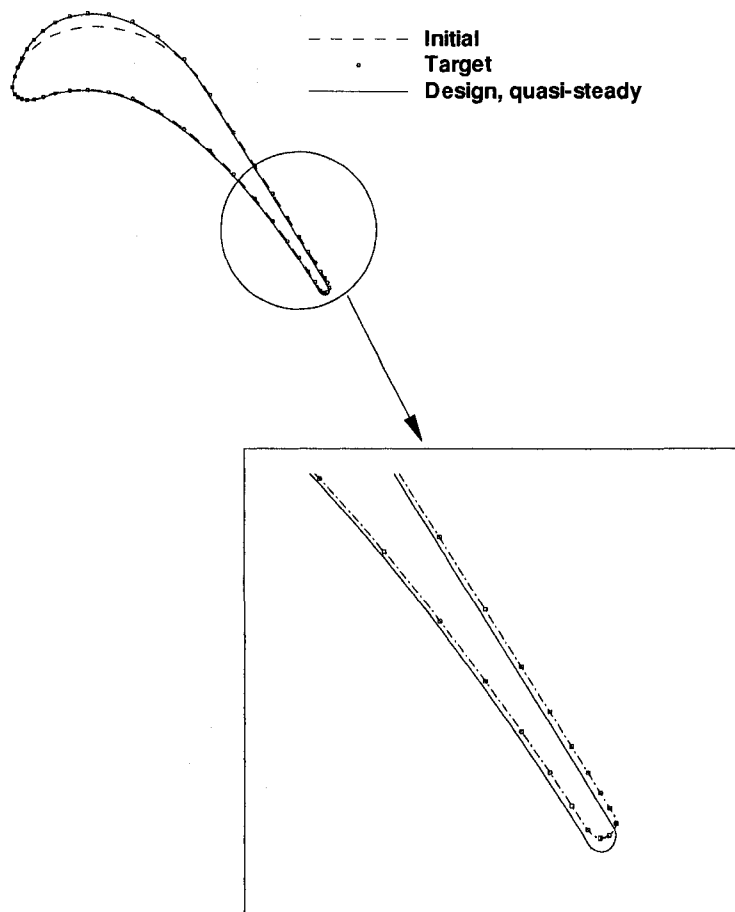
Abbildung 3.6: Initial, target and design rotor geometry near trailing edge where a quasi-steady solution was applied
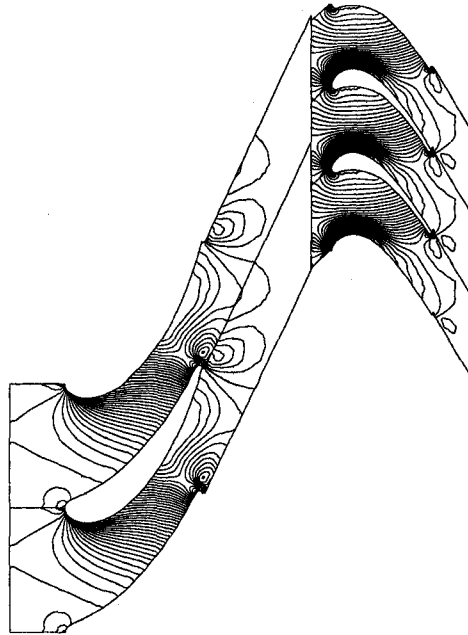
Abbildung 3.7: Isentropic Mach contour lines for the original E/TU-3 stage
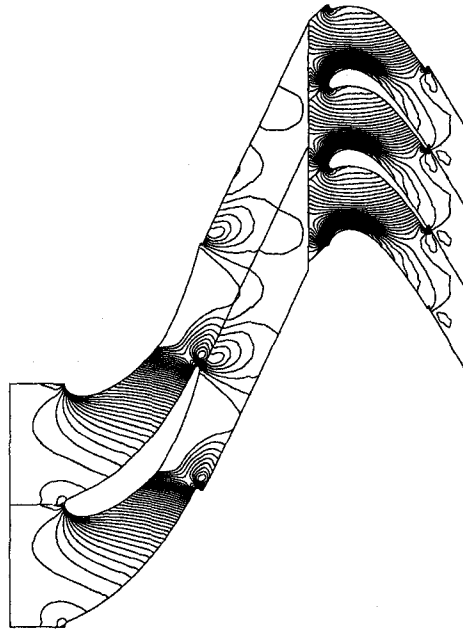
Abbildung 3.8: Isentropic Mach contour lines for the modified E/TU-3 stage
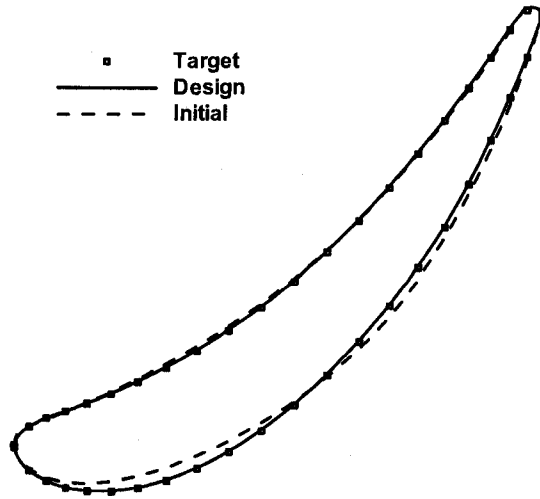
Abbildung 3.9: Initial, target and design stator geometry
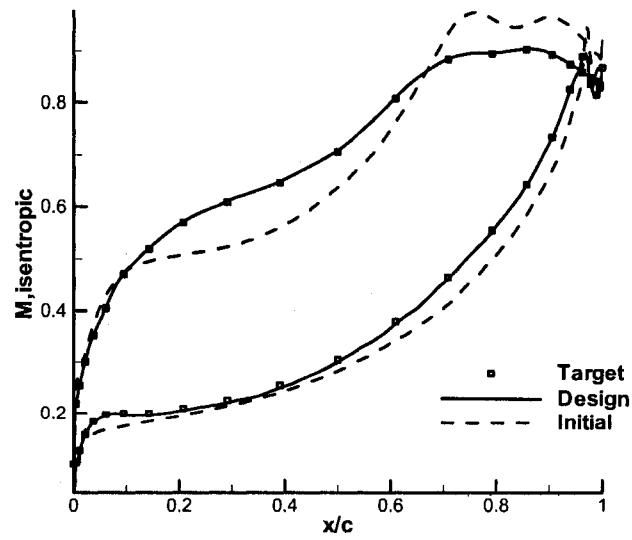
Abbildung 3.10: Initial, target and design stator Mach number distribution

Chapter 4

Redesign Cases

In this chapter three redesign cases are studied and presented. These cases represent single and multistage subsonic turbomachines. A single stage subsonic turbine, called E/TU-3 [52] is addressed first where several distinct redesign scenarios are studied. The second case presents a 2.5 E/TU-4 [52] subsonic turbine and the redesign setting is focused on the second and third stators in order to reduce local suction side diffusion. Finally, an E/CO-5 2.5 stage compressor geometry [52], which is running at an off design operation point, is investigated and redesigned of the first rotor as well as the first and second stators. The goal of these three cases is to improve their performance, e. g. efficiencies and loss coefficients or pressure ratios.

4.1. Redesign of E/TU-3 turbine, part I

Two different redesign scenarios are investigated in this first part. First, the rotor pressure loading is modified while its thickness distribution is fixed which results in a modification of the camber distribution. Second, both stator and rotor pressure loadings are simultaneously modified, while fixing their thickness distribution. The goal is to control the pressure loading so that stage performance is improved and the stage reaction is fixed.

Rotor redesign

The rotor is redesigned by changing the pressure loading distribution while keeping the original blade thickness distribution, mass flow rate and stage reaction. The mass flow rate is controlled by modifying the rotor back pressure [9], which is a boundary condition in the flow simulation; and the reaction is controlled by having the same total pressure loading (given by the area under the original and the target pressure loading curves).

Figure 4.1 shows the original and three suggested pressure loading distributions for the rotor where it is noted that the original blade is front-loaded and the maximum loading is relatively high. The three different loadings are investigated; all of them have about the same total loading (area under the curve), hence same pressure drop across the rotor, which results in approximately the same reaction. The suggested pressure loadings explore the effect of varying the magnitude and location of the maximum loading on the blade performance as well as the acceleration on the last third of the chord. The same camber line shape is maintained in the first and last 2% chord. When the maximum loading is moved downstream, it makes it possible to avoid a large flow acceleration before turning, which results in reducing the diffusion coefficient on the blade suction surface. That, however, can introduce higher pressure loading gradients towards the trailing edge where the local thickness is relatively small. This detail might be important for the blade structural design.

The rotor geometry that satisfies Case 1 target loading distribution and the corresponding pressure distribution and loading are shown in Fig. 4.2, which shows a reduction of suction side diffusion that results in an improvement in loss coefficient and isentropic efficiency. The rotor geometry and the corresponding pressure loading for Case 2 are given in Fig. 4.3 and lead to an increase in total-to-total efficiency of around 0.1% because of the reduced diffusion on the blade suction side. Case 3 is presented in Fig. 4.4 and it shows a performance deterioration as the diffusion

coefficient was larger and slightly shifted downstream. Deviations in mass flow rate and reaction were within acceptable limits in all three cases. The final results of these three cases are summarized in Table 4.1. An efficiency increase was difficult to obtain as the total-to-total efficiency is already at 92.1%. Nevertheless, this parametric study shows clearly the influence of the loading distribution on the blade performance and stage output.

Stage redesign

The E/TU-3 stator and rotor were simultaneously redesigned by changing the pressure loading distribution for both rows. The original mass flow rate and the reaction were kept unchanged. This was accomplished by running the Navier-Stokes program in inverse mode in both stator and rotor regions. Figure 4.5, giving the original and design blade shapes as well as pressure distribution and loading, shows that the prescribed loading between 10% and 60% chord is smoother that the original profile and has a slightly reduced maximum value. For the rotor target loading, the maximum value was reduced and was moved slightly downstream, see Fig. 4.5. The changes in stator and rotor pressure loadings result in a decrease in the suction side diffusion, which results in an improvement in the pressure loss coefficients in both rows and in stage efficiency; Table 4.2 summarizes the results of the stage redesign, note that the original stage is quite efficient.

Figure 4.5 shows that the redesigned rotor and stator profiles are slightly different from the original ones. This slight change in profiles resulted in a reduction in pressure loss coefficients for the stator of 0.1% and rotor of 0.7% and an increase in stage total-to-total efficiency of 0.4%. The design incidence angle did not change as the mass flow and flow Mach number at stator outlet deviated only by about 0.01%. Reaction differed by 1.3%, which is due to the fact that the design total loadings of the stator and rotor are slightly different from the original ones.

4.2. Redesign of E/TU-3 turbine, part II

In the previous section the stage redesign was done for fixed reaction, mass flow rate and blade speed. In this redesign the stage reaction is increased from 0.32 to 0.4 as it is thought that this measure would raise the total-to-total stage efficiency.

This increase in reaction was accomplished through two different scenarios. First, the rotor loading was increased so as to increase the reaction, and therewith to increase the pressure ratio and ideally the total-to-total efficiency. The second case involves a redesign of both stator and rotor where the stator loading is decreased while that of the rotor is increased.

Rotor redesign

The rotor is redesigned by increasing the rotor pressure loading by 10 %. In Fig. 4.6 the target pressure loading is presented. The area gain of the loading curve is focused on 50% chord for both cases. Furthermore the maximum loading is slightly decreased to decrease of the suction side diffusion and thus the rotor loss coefficient. The mass flow is supposed to be constant over the entire design process which is achieved by controlling the stage exit pressure ratio.

After 750 design steps the final geometry was obtained. Figure 4.6 presents the modified rotor geometry and the initial, target, and design isentropic Mach numbers. The suction side diffusion peak was replaced by a nearly constant pressure distribution along the suction side which led to a reduction of diffusion losses of 0.5%. The increase in pressure loading raised the stage pressure ratio by 15%. Although this pressure ratio was increased the efficiency did not drop but was raised by 0.2%. The results are outlined in Tab. 4.3. A further augmentation of the stage pressure ratio without choking the throat is barely possible as the flow is already close to sonic conditions there. Changing the stage pressure ratio generally leads to a shift of the

design operation point as well as the incidence angles of possibly adjacent blade rows which is not always advisable, as a proper stage matching is of the highest importance [53].

Stage redesign

This redesign case has the goal to increase the efficiency by changing the stage reaction at constant pressure ratio. Stator and rotor blade geometries are modified simultaneously in order to increase the stage reaction. To maintain the same pressure ratio the sum of the area under the pressure loading curves of stator and rotor was kept constant. The stator pressure loading was reduced by about 3% and the rotor pressure loading was increased by corresponding 3% (not visible in Fig 4.7 as non-dimensionalized pressures in rotor frame refer to different stagnation pressures). The shape of the loadings were chosen to be similar compared to previous cases in order to take advantage of the flow field improvements on the suction side. The stator loading resembles the one of the stage redesign case where the reaction was kept constant reaction (see Fig. 4.5) but with a reduced area under the loading curve. For the rotor a related pressure loading shape to the previous rotor redesign case was selected (see Fig. 4.3) in order to reduce suction side diffusion.

After 800 design steps the target pressure distributions were achieved. The stage performance is summarized in Tab. 4.4 and Fig. 4.7 shows the finale blade geometries and the corresponding initial, target and design isentropic Mach numbers. Due to the changes in pressure loading the reaction increased by 10 points from 0.32 to 0.42. The combination of decreased pressure loading on the stator side and decreased diffusion losses at the rotor led to an increase of total-to-total efficiency was raised by 0.6% because of the shift in reaction and the accompanied reduction in loss coefficient. The stator coefficient did not change at all and the rotor loss coefficient dropped 0.5%. The conventional practice, founded on turbomachinery theory, would predict a difference

in rotor and stator stagger angles due to the shifted stage reaction [54]. This would hold true if the stagger angle was the only modification on the geometries and the inlet rotor flow angle was constant. However, in these redesign cases the camber line and its inlet and outlet blade angles are locally modified to reach the target pressure distribution. This might implicitly alter the stagger angle but it does not necessarily have to. Furthermore, in the present case the rotor inlet flow angle is deviating from the original value due to the change in stator loading.

4.3. Redesign of E/TU-4 2.5 stage turbine

In this section the E/TU-4 2.5 stage subsonic turbine are redesigned. The results of the analysis of this case are presented in Appendix C. Figure 4.8 shows the pressure distributions of all five blade rows of the E/TU-4 turbine. Rotors 1 and 2 are showing a decent pressure distribution without any pronounced diffusion regions or an inconvenient suction side flow behavior. The redesign of the 2.5 stage turbine focuses on the second and third stator blade rows. Figure 4.8 depicts the pressure distributions along the five blade rows. It can be seen that the 2nd and 3rd stators have a pronounced diffusion region on the blade suction side in the last 20% chord (see Figs. 4.9 and 4.10). The 1st stator shows a slight diffusion region which is not as pronounced as for the other two stators downstream (Figure 4.9) and therefore, it is not regarded.

To compare the original and the redesigned turbine, a multistage loss coefficient was defined as:

$$\zeta = 1 - \frac{1 - \left(\frac{p_5}{p_{o5}}\right)^{\frac{\gamma-1}{\gamma}}}{1 - \left(\frac{p_5}{p_{o1}}\right)^{\frac{\gamma-1}{\gamma}}} \tag{4.1}$$

where 5 refers to the position at outlet of the third stator. This coefficient reflects the losses caused by the boundary layer, diffusion and 2D mixing.

In order to reduce the suction side diffusion the blade pressure loading was

selected as design variable in combination with a retained tangential thickness distribution. For both stators the maximum loading was decreased and the loading was slightly increased in the first half of the blade. Figures 4.9 and 4.10 present the initial, target and design pressure distributions based on the target pressure loading for stators 2 and 3.

During the first few design steps, the relaxation factors for grid displacement and virtual velocity were given a low value to prevent high initial mesh velocity gradients. This problem is similar to the one given in the second part of the E/TU-4 redesign where the reaction was supposed to increase. In the present case the stage reaction should not change but a sudden start of blade movement causes substantial changes in the flow field which are propagating up- and downstream to the adjacent blade rows. These unintended flow field changes coming from a neighboring blade row decrease the global convergence rate and affect negatively the inverse procedure at the next design step.

The variations in mass flow can be reduced by fixing the inlet mass flow rate at the turbine inflow plane. Hence, the total pressure varies implicitly and no further intervention in the design process to stabilize the mass flow rate is needed. This procedure can be recommended if the reaction in every single stage is not supposed to vary much during the design process and therefore just for minor corrections of a loading distribution. As the changes in pressure loading were rather substantial for both stator blade rows, a constant reaction during the design process could not be guaranteed. Therefore, instead of fixing the reduced mass flow at inlet, the back pressure was adjusted very carefully to maintain a constant mass flow rate.

After about 1400 design steps, which takes twice the computing time of one analysis, the design process converged, i.e. the difference between the target and computed pressure loading was within an acceptable tolerance. Figures 4.9 and 4.10 present the initial, target and resulting pressure distributions of the redesigned stators. It can

be seen that the pressure diffusion regions on the suction side were reduced, which was the primary design intent. The modifications in blade geometry can be depicted in Figs. 4.9 and 4.10, respectively. Table 4.5 shows the design flow conditions and the deviations from the initial set up. The flow angles changed slightly due the small change in pressure loading of the second and third stators. The difference in mass flow rate between original and design multistage was 0.05% The multistage loss coefficient ζ dropped from 0.072 to 0.066 which was less than expected. Furthermore, the exit pressure ratio at the 3rd stator was increased by 1.9%. In summary, this exercise demonstrates the ability of this inverse method to achieve a prescribed pressure loading when several blade rows are simultaneously redesigned in a multistage environment and by carefully tailoring the blading it was possible to further improve an already well designed multistage turbine.

4.4. Redesign of E/CO-5 2.5 stage compressor fan

A 2.5 stage compressor represents the last redesign case in this work. The geometric characteristics of this compressor stage are given in Table 4.6. Originally, this stage was supposed to run at an inlet Mach number of around 0.07 [52, 55]. Attempts failed to obtain decent analysis results as the present flow solution scheme performs rather poorly at such low Mach numbers and would need to be preconditioned for low Mach number flows [56]. For that reason, an operating point where the flow Mach number is around 0.3 was chosen for the redesign exercise. This off-design point was reached by increasing the blade speed and back pressure. In Table 4.7 the performance characteristics of that operating design point are presented.

A hybrid mesh, similar to the one which was used for the E/TU-3 case, was applied for all five blade rows. An unstructured mesh using Delauny triangulation was used for the interior flow field and an unstructured O-mesh was constructed around

the blade surfaces so as to properly resolve the boundary layer and to ensure that the average y+ < 1 near the blade surface. The inlet guide vane (IGV) and second stator were meshed with about 12500 nodes (23200 cells). The grid of the first and second rotor as well as the first stator consisted of about 9800 nodes (17100 cells).

The growth in endwall boundary layer in the annulus was again not taken into account. Hub and tip radii are not varying in the axial or circumferential direction. As the IGV geometry was not available the stator geometry was used, which provided the first rotor with satisfying inlet flow angles [55]. Furthermore, the IGV is not object of investigation in this report and hence an exact representation of its geometry is not critical. Figure 4.11 represents the multistage blade row assembly showing the corresponding pressure distributions.

This 2.5 stage compressor redesign focuses on the first stage, namely first rotor (R1) and first stator (S1), as well as the second stator (S2). At the 2nd stator there is a pronounced suction side separation region within the last 25% chord which can be seen in Fig. 4.15. The goal was to remove, or at least weaken, this recirculating flow region near the TE of S2. As the diffusion factor [57] was low (0.1) for all five blade rows, the prescribed loading was increased for R1, S2 and especially S1. The pressure loss should not substantially increase until a diffusion coefficient of 0.5 is reached which can be barely reached at the present design conditions. Figures 4.12, 4.13, 4.14 present the initial, target and design pressure loadings of R1, S1 and S2. The loading of R1 was increased in order to raise the incidence angle at the downstream stator S1. It can be seen that the maximum loading near the LE of R1 and S1 was increased and at S2 the total loading given by the area under the curve and its slope towards the TE was slightly raised. The latter measure was supposed to reduce the recirculation near the TE. The back pressure was adjusted to assure a minimum deviation of the mass flow rate over the entire design process.

After 900 design steps the target pressure loadings were reached. Figures 4.12,

4.13, 4.14 present the modified blade geometry and the initial, target, and design isentropic Mach numbers. As the loading was increased on three blades the pressure jumped from 1.48 to 1.55 which is equal to an increase of about 5%. The mass flow deviation was less then 0.15%. Table 4.8 compares the pressure ratios and loss coefficient of the design with the original multistage. The suction side separation at the second stator was reduced from 25% chord to 15% chord (Fig. 4.15) which caused a drop in the enthalpy loss coefficient of about 0.3%. The loss coefficients of the other blades increased slightly as their loading was increased. The total-to-total efficiency was increased by 0.7%. Once again, by properly tailoring the blade loading, based on design experience, it was possible to improve the compressor performance.

Tabelle 4.1: E/TU-3, Part I: Rotor design summary

	Original	Case 1	Case 2	Case 3
ζ_{rotor}	6.6%	5.9%	6.4%	6.6%
η_{t-t}	92.1%	92.2%	92.2%	91.9%
Mass flow deviation	—	0.08%	0.11%	0.09%

Tabelle 4.2: E/TU-3, Part I: Stage design summary

	Original	Design
ζ_{stator}	5.4%	5.3%
ζ_{rotor}	6.6%	6.0%
$\alpha_{2,stator}$	67.9°	68.0°
$\alpha_{1,rotor}$	44.7°	44.2°
η_{t-t}	92.1%	92.5%
Mass flow deviation	—	0.05%
Reaction	0.32	0.33

Tabelle 4.3: E/TU-3, Part II: Rotor design summary

	Original	Design
ζ_{rotor}	6.6%	5.9%
η_{t-t}	92.1%	92.4%
Mass flow deviation	—	0.05%
Reaction	0.32	0.43
Pressure ratio PR	1.784	1.887

Tabelle 4.4: E/TU-3, Part II: Stage design summary

	Original	Design
ζ_{stator}	5.4%	5.4%
ζ_{rotor}	6.6%	5.9%
$\alpha_{2,stator}$	67.9°	67.1°
$\alpha_{1,rotor}$	44.7°	41.4°
η_{t-t}	92.1%	92.6%
Mass flow deviation	–	0.05%
Reaction	0.32	0.42

Tabelle 4.5: E/TU-4 Multistage design summary

	Original	Design
$\alpha_{1,stator2}$	97.7°	93.9°
$\alpha_{1,stator3}$	95.3°	95.8°
Mass flow deviation	–	0.05%
Exit pressure ratio $[p_5/p_{01}]$	0.38	0.387
Exit Mach number	0.73	0.72
ζ	7.2%	6.7%

Tabelle 4.6: E/CO-5 stage geometric characteristics

	IGV	R1	S1	R2	S2
Chamber angle θ	17°	17°	20°	17°	20°
Stagger angle ξ	14°	48°	35°	45°	35°
Number of blades	55	44	44	44	44
Axial chord-to-pitch ratio	1.2	1.33	1.33	1.33	1.33
Aspect ratio	1.92	1.92	1.92	1.92	1.92
Axial gap to stator chord	0.2	0.19	0.18	0.19	-

Tabelle 4.7: E/CO-5 off-design operation point

	IGV	R1	S1	R2	S2
Incidence i	0°	0°	3°	4°	5°
Inlet Mach numbers	0.31	0.33	0.45	0.30	0.46
General conditions					
Blade speed $\frac{U}{\sqrt{RT_{01}}}$	0.733				
Mass flow rate $\frac{\dot{m}\sqrt{RT_{01}}}{P_{01}}$	0.220				

Tabelle 4.8: E/CO-5 Multistage design summary

	IGV	R1	S1	R2	S2
static PR, (p_n/p_{n+1}),original	0.98	1.14	1.07	1.12	1.08
static PR, (p_n/p_{n+1}),design	0.98	1.14	1.09	1.14	1.10
ζ , original	0.006	0.026	0.051	0.049	0.107
ζ , design	0.006	0.031	0.050	0.055	0.075
	original	design			
Overall static pressure ratio	1.48	1.55			
η_{t-t}	0.877	0.884			
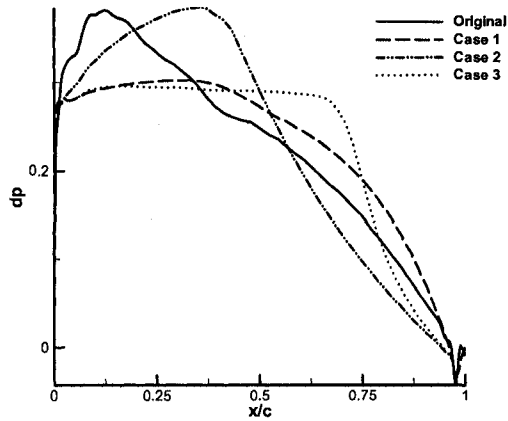
Abbildung 4.1: Rotor redesign: original and target pressure loadings
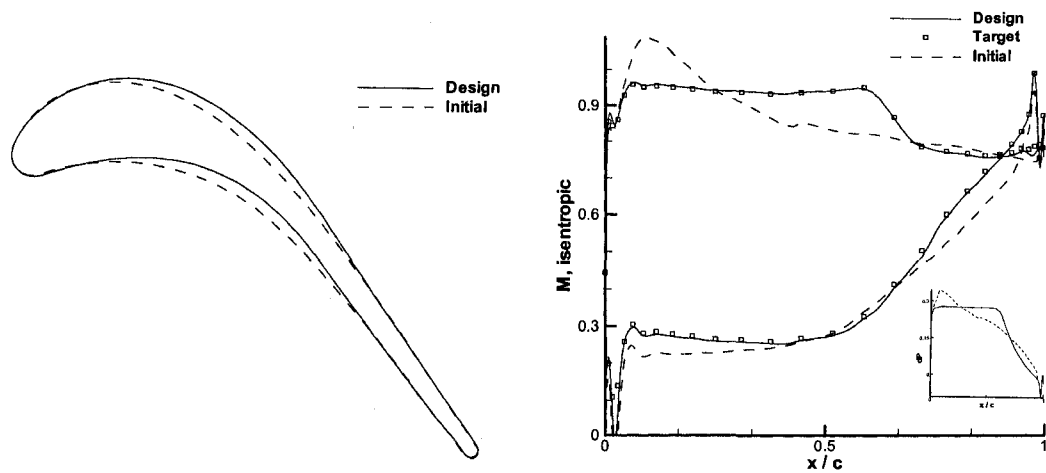
Abbildung 4.2: E/TU-3, part I, Case 1: Rotor geometry, isentropic Mach number and pressure loading
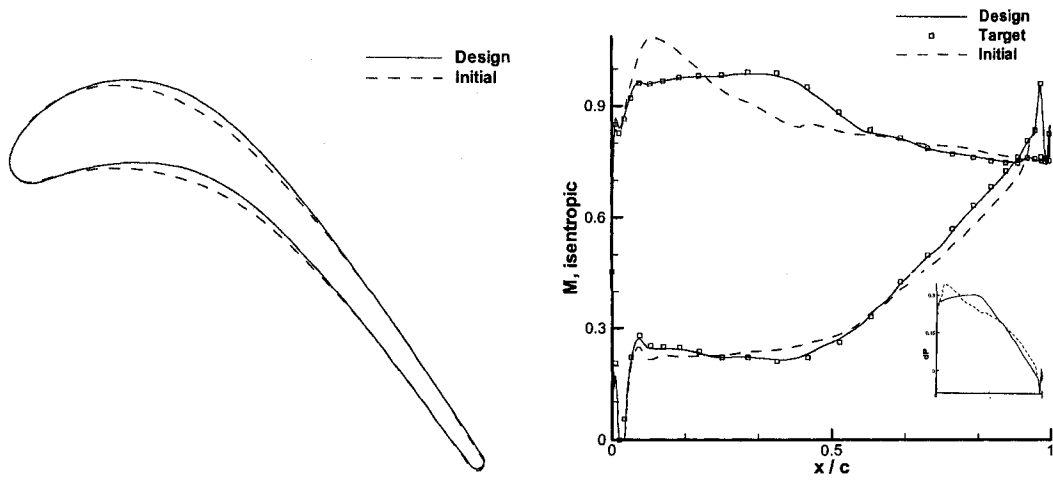
Abbildung 4.3: E/TU-3, part I, Case 2: Rotor geometry, isentropic Mach number and pressure loading
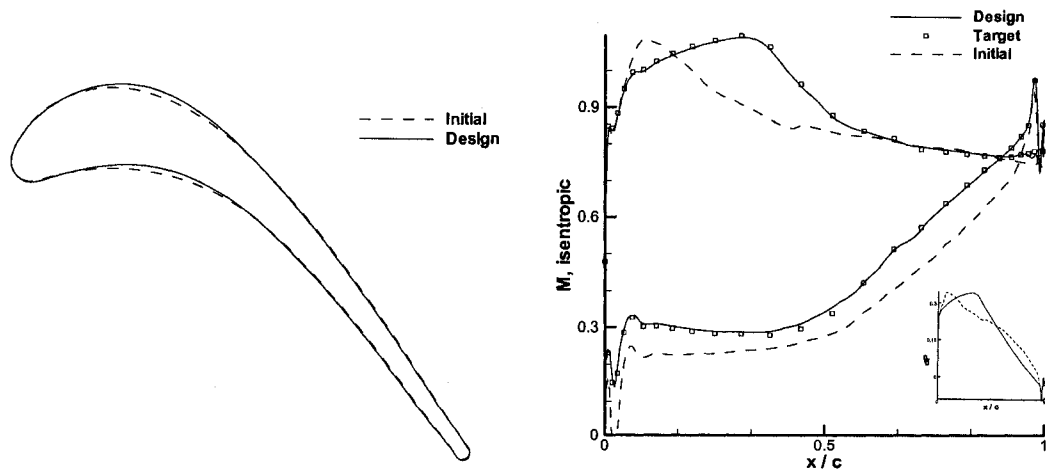
Abbildung 4.4: E/TU-3, part I, Case 3: Rotor geometry, isentropic Mach number and pressure loading
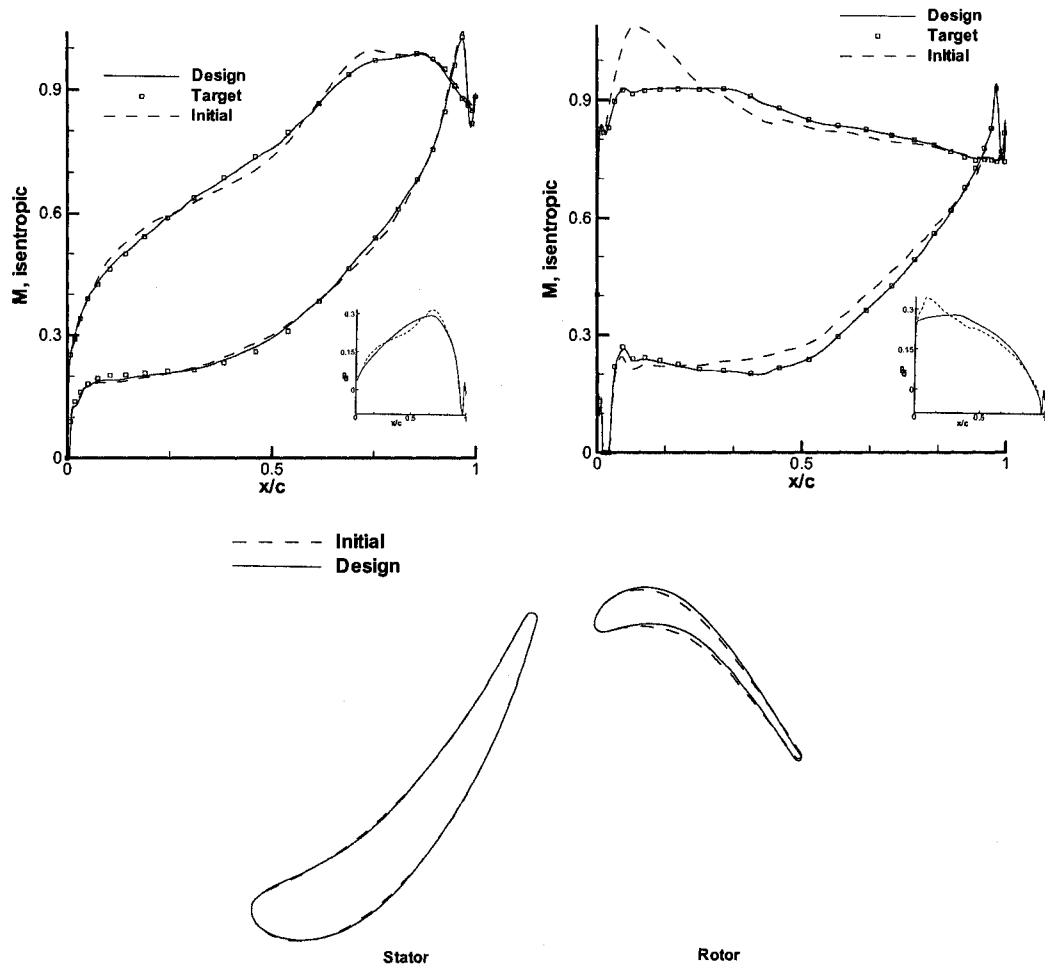
Abbildung 4.5: E/TU-3, part I, Stage case: Stator and rotor isentropic mach number and pressure loading, stator and rotor geometry
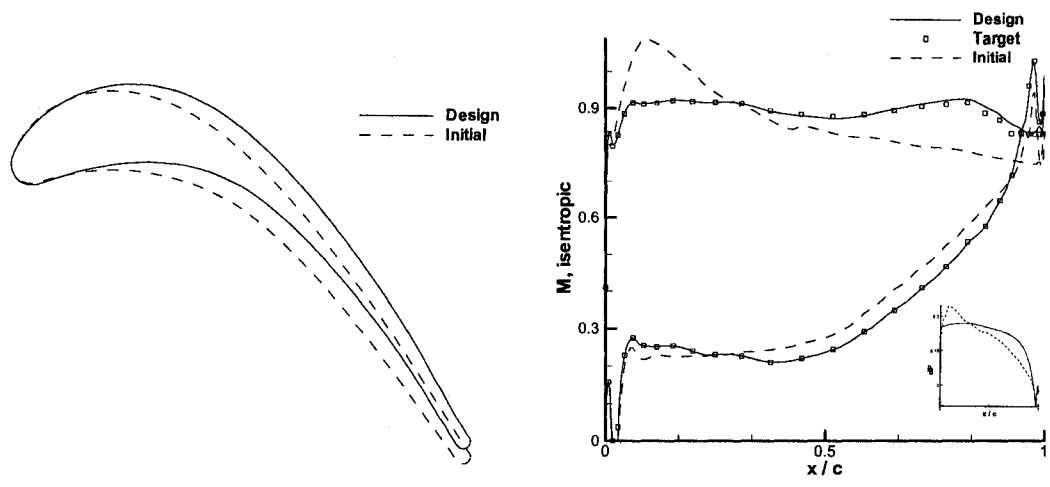
Abbildung 4.6: E/TU-3, part II, Rotor case: Rotor geometry, isentropic Mach number and pressure loading
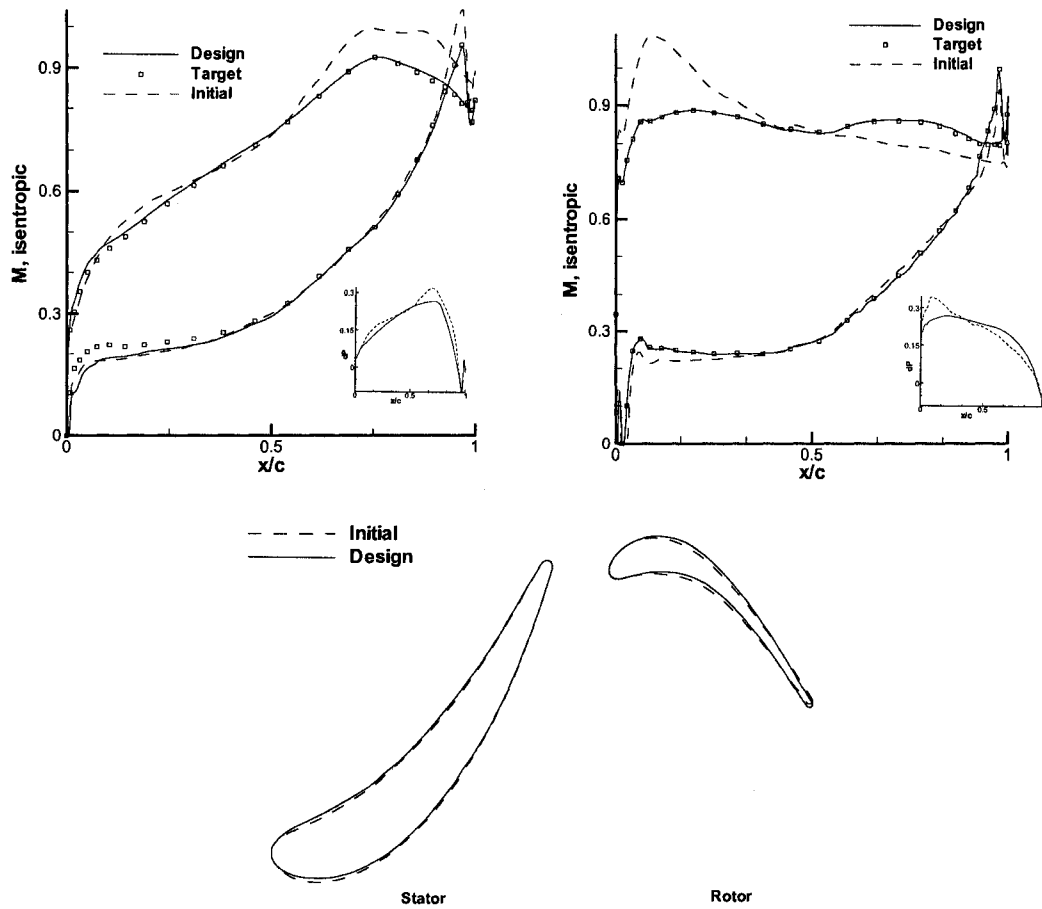
Abbildung 4.7: E/TU-3, part II, Stage case: Stator and rotor isentropic mach number and pressure loading (bottom right corner), stator and rotor geometry
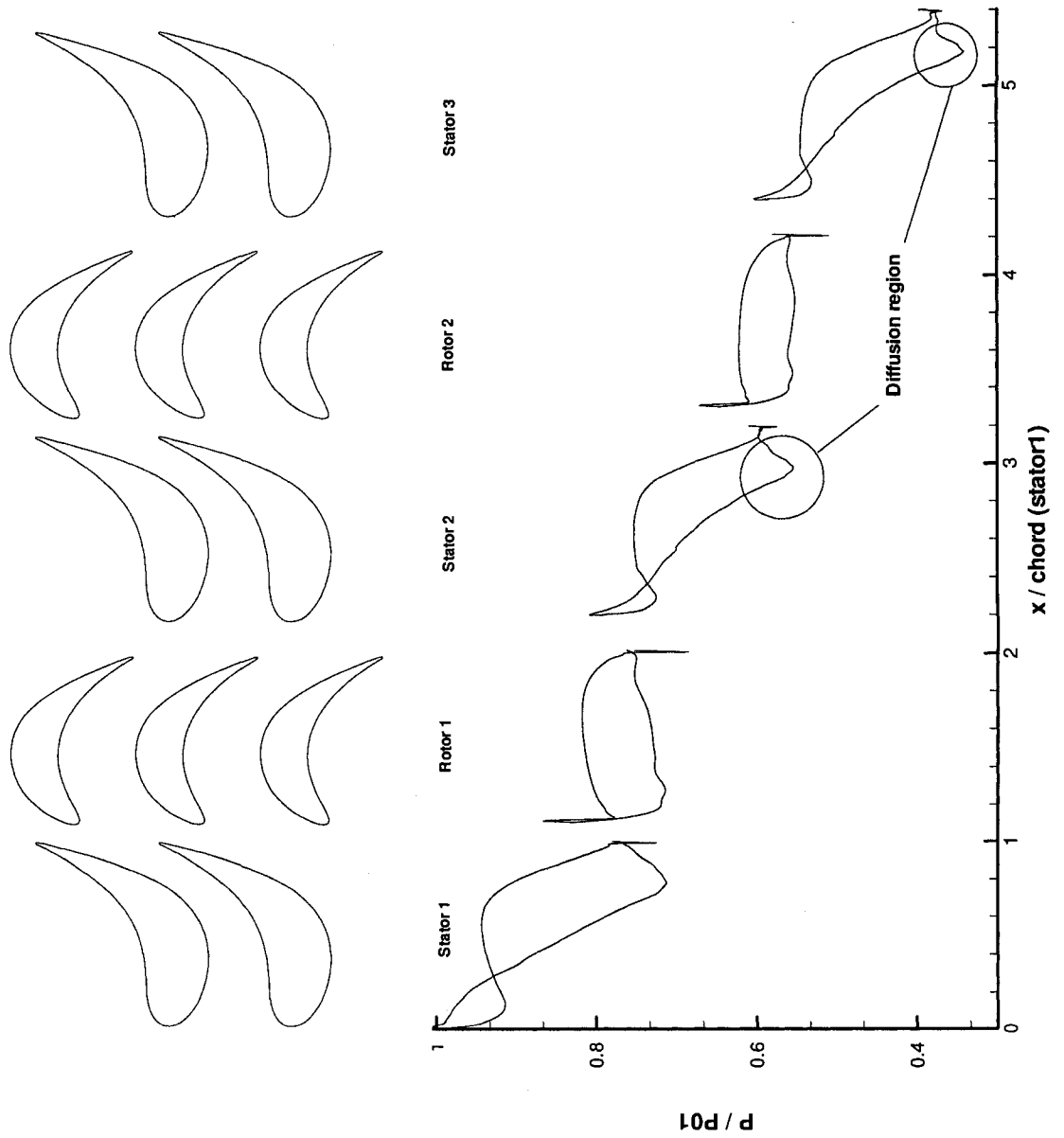
Abbildung 4.8: Multistage blading and pressure distributions
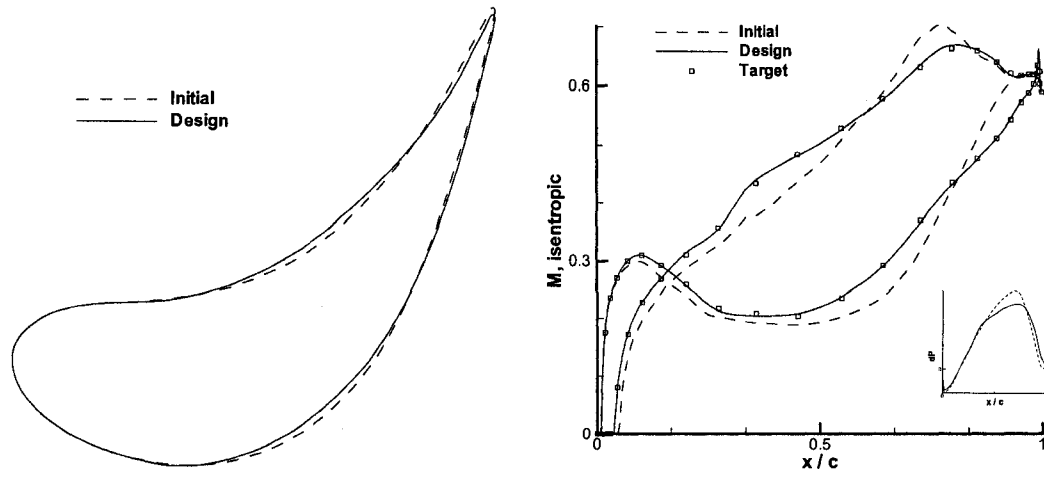
Abbildung 4.9: E/TU-4, Stator 2: Stator geometry, isentropic Mach number distribution and pressure loading
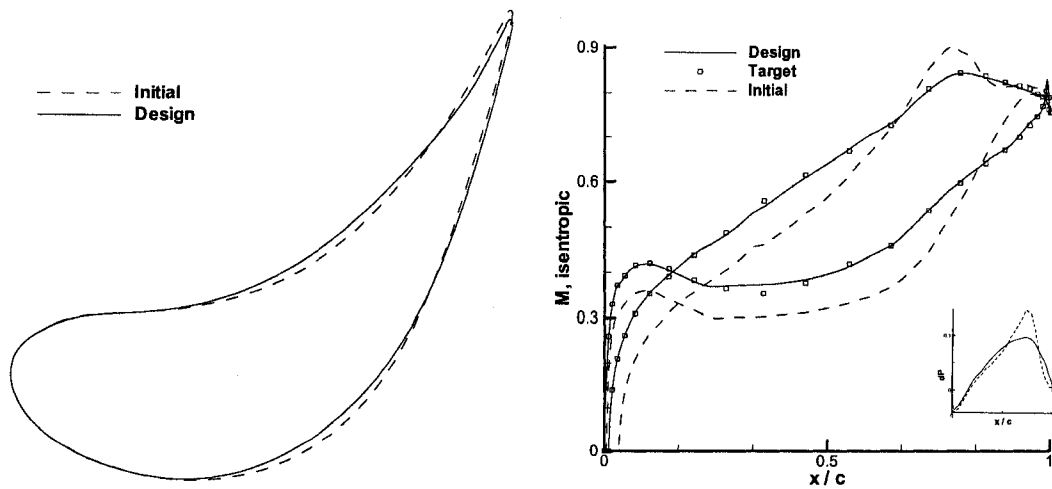
Abbildung 4.10: E/TU-4, Stator 3: Stator geometry, isentropic Mach number distribution and pressure loading
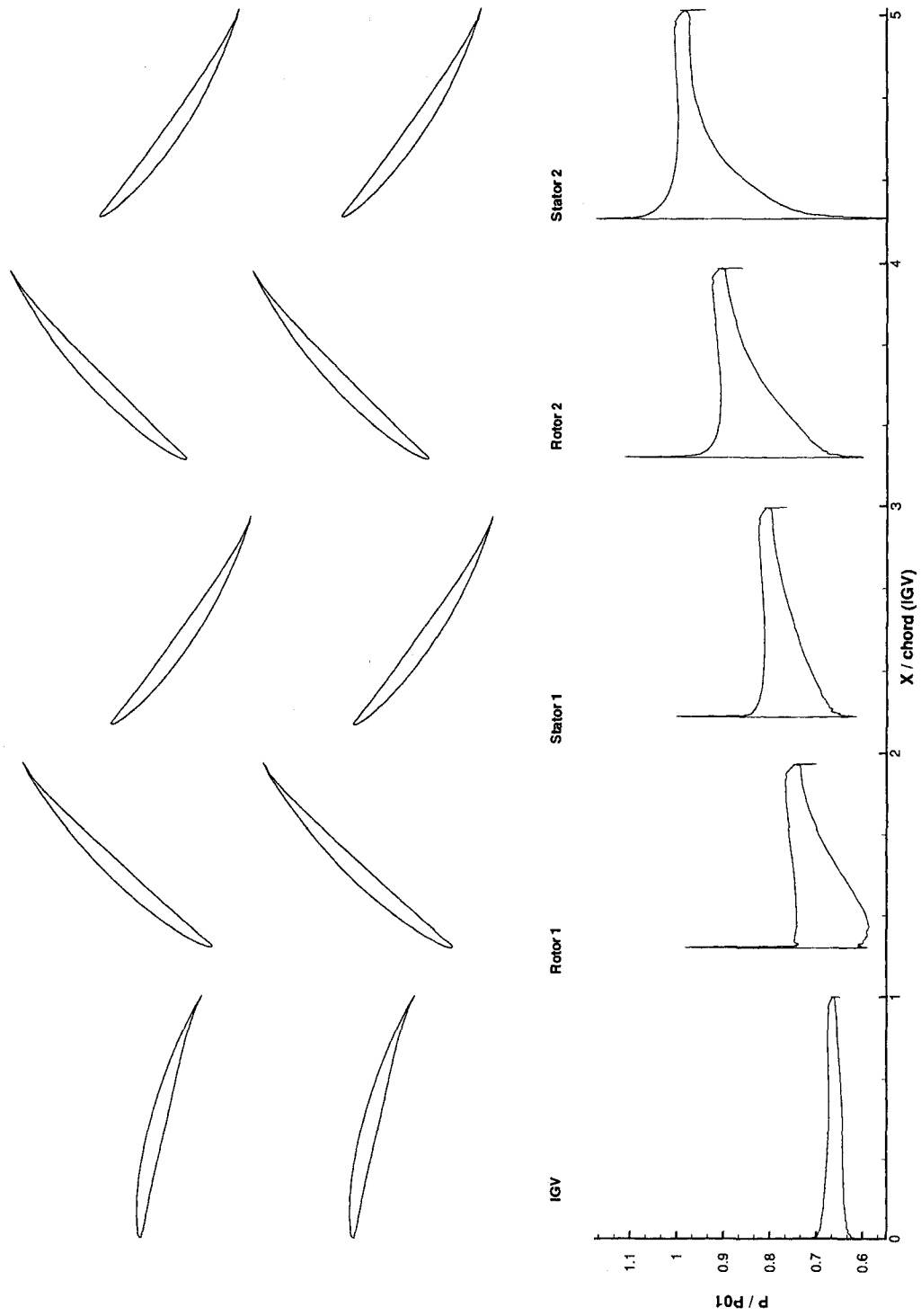
Abbildung 4.11: Multistage blading and pressure distributions

70
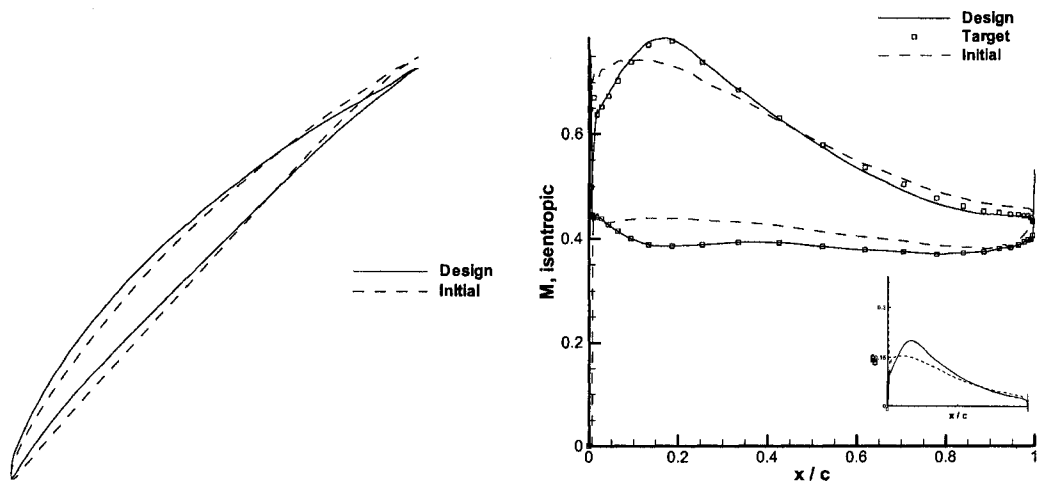
Abbildung 4.12: E/CO-5, Rotor 1: Rotor geometry, isentropic Mach number distribution and pressure loading
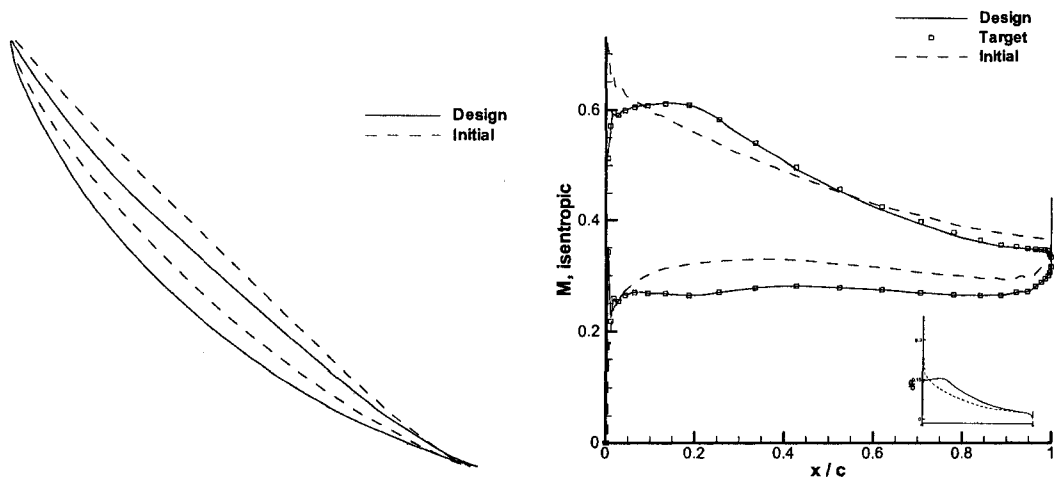
Abbildung 4.13: E/CO-5, Stator 1: Stator geometry, isentropic Mach number distribution and pressure loading
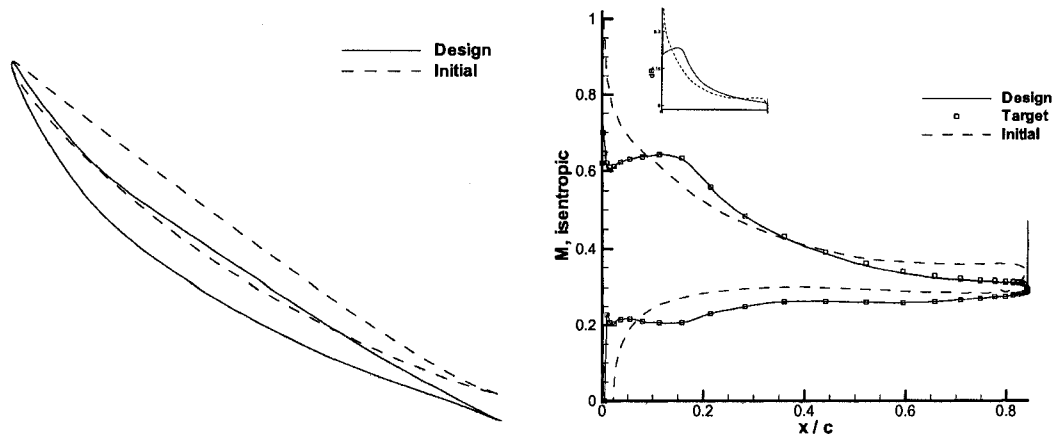
Abbildung 4.14: E/CO-5, Stator 2: Stator geometry, isentropic Mach number distribution and pressure loading
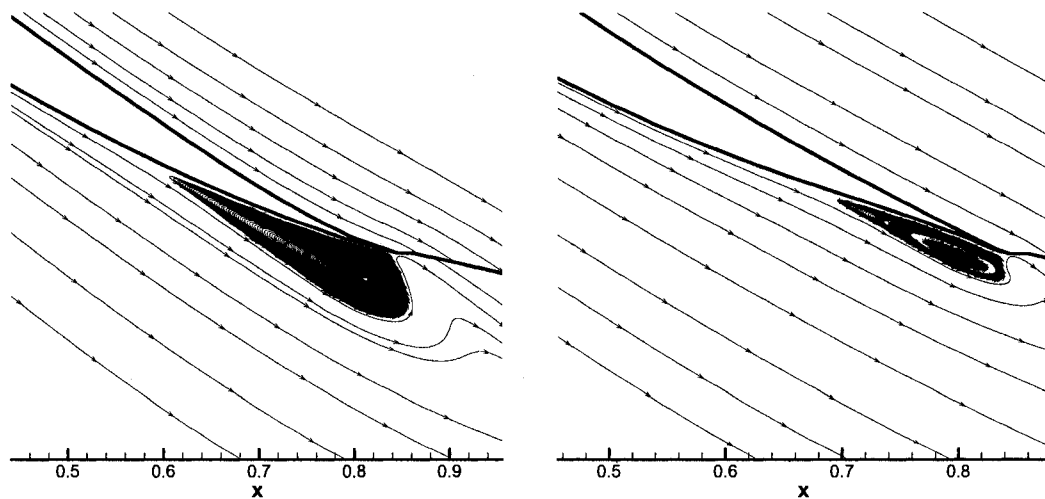
Abbildung 4.15: E/CO-5, Stator 2: Recirculation zones on suction side of second stator, left: initial, right: redesigned
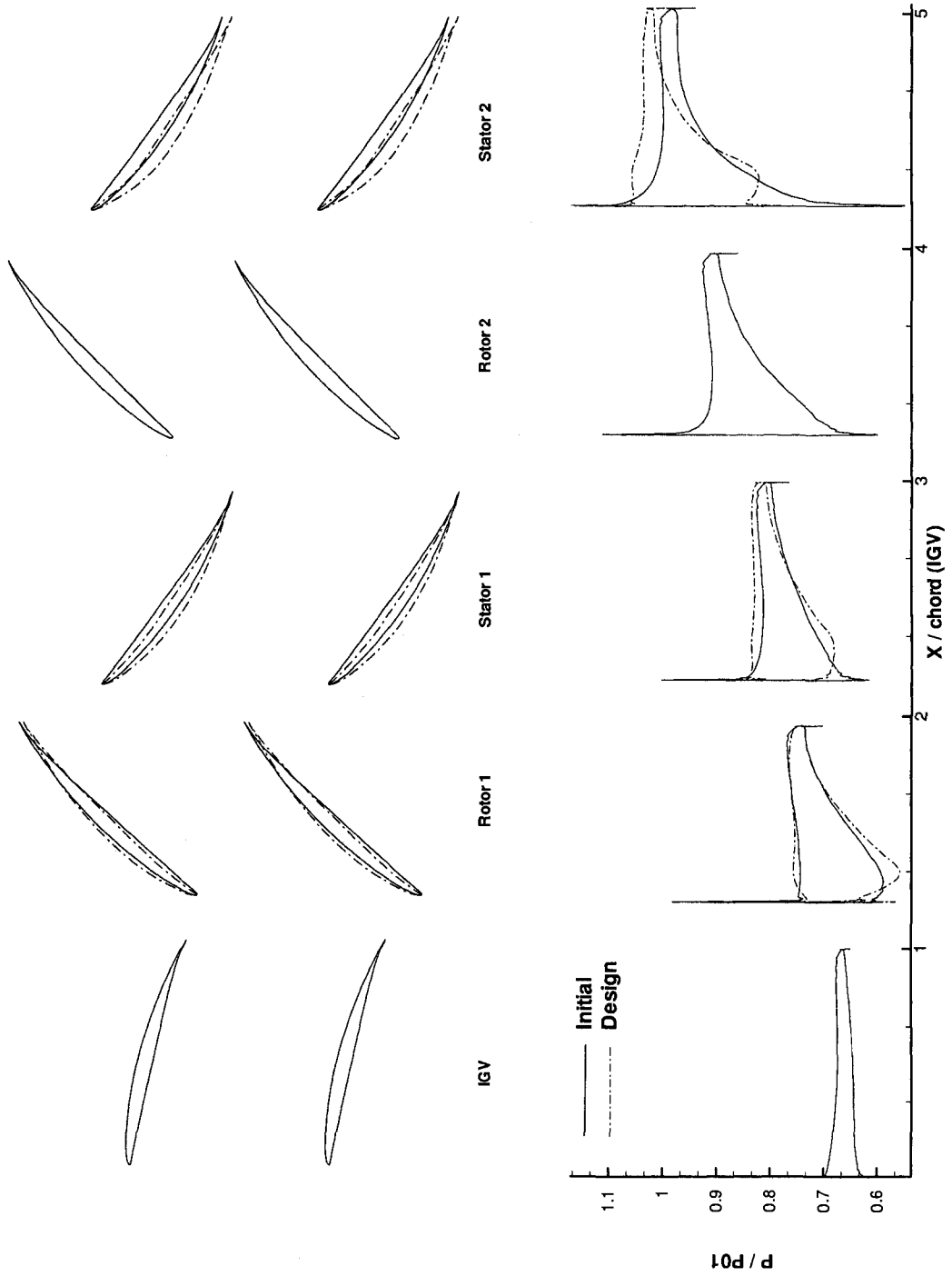
Abbildung 4.16: Multistage blading and pressure distributions, initial& design

Chapter 5

Conclusion

5.1. Summary

The present aerodynamic inverse design method has been successfully extended from linear 2D cascade to 2D and quasi 3D multistage application. In that method, the pressure distribution on the blade surfaces or alternatively, the blade loading and their thickness distribution were employed as design variables and the blade shape was modified using a virtual wall movement. The virtual velocity distribution, which was derived from the balance of design and target transient momentum fluxes, was calculated from the current and the target pressure distribution on the blade surfaces. NRBCs and steady mixing planes were implemented in order to apply the existing method to multistage applications. The unsteady RANS equations, which were blended with a quasi 3D formulation to account for axial variations of the streamtube thickness, were solved in a time-accurate fashion.

The method was validated for two different subsonic turbines and the results indicate that the method is robust and capable of recovering blade geometries and stage performances. Three redesign cases gave a demonstration of the usefulness of this inverse method. The E/TU-3 turbine case was successfully redesigned in

scenarios where pronounced and carefully tailored pressure loadings and hence geometry modifications on both stator and rotor led to a considerable increase of stage efficiency. Simultaneous redesign of two stators of E/TU-4 2.5 stage turbine reduced efficiently the local suction side diffusion leading to a reduction of the profile losses. In the last case three blades of the E/CO-5 2.5 stage compressor fan were simultaneously redesigned in order to increase the stage pressure ratio and to reduce the separated flow region at the suction side of the second stator. Once again these goals were achieved due to elaborated pressure loading modifications.

The method is capable of leading the performance of single and multistage turbomachines to higher levels by reshaping multiple blade geometries simultaneously in order to match a prescribed pressure loading. Diffusion regions can be effectively removed or weakened but the merits of the methods are especially demonstrated in regions where the flow is rather largely separated. Experienced designers can use this inverse method efficiently to improve the performance of a multistage turbomachinery blading.

5.2.   Future work

The following improvements should be considered to enhance its attractiveness as a blade design tool:

- The development of a 3-D RANS solver or the implementation of the method into existing 3-D RANS-solver is necessary to bring the method to the next level. On basis of the present code the extension to multistage 3-D is possible where the boundary conditions would be implemented in a fully 3-D or at least quasi 3-D fashion.

- In order to control the mass flow rate through a multistage more efficiently, advanced algorithms which are based on control theory are necessary to adjust

the back pressure accordingly.

- Instead of using a preserved tangential thickness distribution, the thickness normal to the camber line should be applied, especially on blade rows with high stagger angles.

Bibliography

[1] S. Pierret, A. Demeulenaere, B. Gouverneur, C. Hirsch, and R. van den Braem-bussche, "Designing turbomachinery blades with the function approximation concept and the navier-stokes equations," *AIAA paper 00-4879*, 2000.

[2] M. Nemec and D. Zingg, "Towards efficient shape optimization based on navier-stokes equations," *AIAA paper 2001-2532*, 2001.

[3] T. Mengistu and W. Ghaly, "Single and multipoint shape optimization of gas turbine blade cascades," *AIAA paper 2004-4446*, 2004.

[4] A. Oyama and M. Liou, "Multiobjective optimization of multi-stage compressor using evolutionary algorithm," *AIAA paper 2002-3535*, 2002.

[5] W. Thompkins and S. Tong, "Inverse or design calculation for nonpotential flows in turbomachinery cascades," *ASME Journal of Engineering for Power*, vol. 104, no. 4, pp. 281–285, 1982.

[6] L. Zannetti, "A natural formulation for the solution of two-dimensional or axisymmetric inverse problems," *International Journal for Numerical Methods in Engineering*, vol. 22, 1986.

[7] M. Giles and M. Drela, "Two dimensional transonic aerodynamic design method," *AIAA Journal*, vol. 25(9), pp. 1199–1205, 1987.

[8] A. Demeulenaere, O. Leonard, and R. Van den Braembussche, "A two-dimensional navier-stokes inverse solver for compressor and turbine blade dasign," *Proceedings of the Institution of Mechanical Engineers, PART A.*, vol. 211, pp. 299–307, 1997.

[9] L. de Vito, R. V. den Braembussche, and M. Deconinck, "A novel two-dimensional viscous inverse design method for turbomachinery blading," *Journal of Turbomachinery*, vol. 125, pp. 310–316, 2003.

[10] O. Leonard and R. van den Braembussche, "Design method for subsonic and transonic cascades with the prescribed mach number distribution," *Transaction ASME*, vol. 114, no. 3, pp. 553–560, 1992.

[11] L. Zannetti and M. Pandolfi, "Inverse design techniques for cascades," *NASA CR-3836*, 1984.

[12] T. Dang, "Inverse method for turbomachinery blade using shock-capturing techniques," *AIAA Paper 95-2465*, 1995.

[13] S. Damle, T. Dang, J. Stringham, and E. Razinsky, "Practical use of a 3d viscous inverse method for the design of compressor blade," *Journal of Turbomachinery*, vol. 121, pp. 321–325, 1999.

[14] M. Ahmadi and W. Ghaly, "Aerodynamic design of turbomachinery cascades using a finite volume method on unstructured meshes," *Journal of Inverse Problems in Engineering*, vol. 6, pp. 281–298, 1998.

[15] B. Choo and M. Zangeneh, "Development of an (adaptive) unstructured 2-d inverse design method for turbomachinery blades," *ASME paper GT2002-30620*, 2002.

[16] M. van Rooij, T. Dang, and L. Larosiliere, "Improving aerodynamic matching of axial compressor blading using a three-dimensional multistage inverse design method," *Journal of Turbomachinery*, vol. 129, no. 1, pp. 108–118, 2007.

[17] T. Yang and F. Ntone, "Viscous compressible flow direct and inverse computation with illustration," *NASA-CR-175037*, 1986.

[18] S. Tong and W. Thompkins, "A design calculation procedure for shock-free or strong passage shock turbomachinery cascades," *ASME Paper 82-GT-220*, 1982.

[19] K. Daneshkhah and W. Ghaly, "Aerodynamic inverse design for viscous flow in turbomachinery blading," *AIAA Journal of Propulsion and Power*, vol. 23, no. 4, pp. 814–820, 2007.

[20] K. Daneshkhah and W. Ghaly, "An inverse blade design method for subsonic and transonic viscous flow in compressors and turbines," *Journal of Inverse Problems in Science and Engineering*, vol. 14, no. 3, pp. 211–231, 2006.

[21] K. Daneshkhah and W. Ghaly, "Redesign of a highly loaded transonic turbine nozzle blade using a new viscous inverse design method," *ASME paper GT2007-27430*, 2007.

[22] V. Mileshin, I. Orekhov, S. Shchipin, and A. Startsev, "3d inverse design of transonic fan rotors efficient for a wide range of rpm," *ASME paper GT2007-27817*, 2007.

[23] M. Giles, "Unsflo: A numerical method for the calculation of unsteady flow in turbomachinery," *MIT Report No. 205*, 1991.

[24] M. Giles, "Nonreflecting boundary conditions for euler equation calculations," *AIAA Journal*, vol. 28, no. 12, pp. 2050–2058, 1990.

[25] R. Chima, "Calculation of multistage turbomachinery using steady characteristic boundary conditions," *AIAA Paper 98-0968*, 1998.

[26] R. Merz, J. Kruckels, J. Mayer, and H. Stetter., "Computation of three dimensional viscous transonic turbine stage flow including tip clearance effects," *ASME 95-GT-76*, 1995.

[27] W. D. Dawes, "Towards improved throughflow capability: The use of 3d viscous solvers in a multistage environment," *ASME paper 90-GT-18*, 1990.

[28] J. Yao, R. Davis, J. Alonso, and A. Jameson, "Unsteady flow investigations in an axial turbine using the massively parallel flow solver tflo," *AIAA, Aerospace Science Meeting and Exhibit, Reno*, 2001.

[29] A. Arnone and R. Pacciani, "Rotor-stator interaction analysis using the navier-stokes equations and a multigrid method," *ASME paper 95-GT-177*, 1995.

[30] S. Clark and C. Hall, "A time linearized navier-stokes analysis of stall flutter," *ASME Journal of Turbomachinery*, vol. 122, pp. 467–376, 2000.

[31] P. Cinnella, P. de Palma, G. Pascazio, and M. Napolitano, "A numerical method for turbomachinery aeroelasticity," *ASME Journal of Turbomachinery*, vol. 126, pp. 310–316, 2004.

[32] R. Bladh and C. Pierre, "Dynamic response prediction for a mistuned industrial turbomachinery rotor using reduced-order modelling," *ASME Journal of Turbomachinery*, vol. 124, pp. 311–324, 2004.

[33] B. Baldwin and H. Lomax, "Thin layer approximation and algebraic model for separated turbulent flows," *AIAA Paper 78-257*, 1978.

[34] D. Mavripilis, "Turbulent flow calculations using unstructured and adaptive meshes," *International Journal for Numerical Methods in Fluids*, vol. 91, no. 13, pp. 1131–1152, 1991.

[35] D. Mavriplis, A. Jameson, and L. Martinelli, "Multigrid solution of the navier stokes equations on triangular meshes," *AIAA Paper 89-0120*, 1989.

[36] A. Jameson, "Time dependent calculations using multigrid, with application to unsteady flow past airfoils and wings," *AIAA Paper 91-1596*, 1991.

[37] I. Demirdzic and M. Peric, "Space conservation law in finite volume calculations of fluid flow," *International Journal for Numerical Methods in Fluids*, vol. 8, pp. 1037–1050, 1988.

[38] B. Lakshminarayana, *Fluid Dynamics and Heat Transfer of Turbomachinery*. John Wiley and Sons, 1996.

[39] E. Hall, D. Topp, N. Heidegger, G. McNulty, K. Weber, and R. Delaney, "Investigation of acvanced conterrotation blade configuration concepts for high speeds turboprob systems: Task vii - endwall treatment inlet flow distortion analysis final report," *NASA CR-195468*, 1996.

[40] M. Hathaway and J. Wood, "Application of a multiblock cfd code to investigate the impact of geometry modeling on centrifugal compressor flow field predictions," *Journal of Turbomachinery*, vol. 119, pp. 820 –830, 1997.

[41] W. Shen and J. Sorensen, "Quasi-3d navier-stokes model for a rotating airfoil," *Journal of Computational Physics*, vol. 150, no. 2, pp. 518–548, 1999.

[42] C. Vuillez and J.-P. Veuillot, "Quasi 3d viscous flow computations in subsonic and transonic turbomachinery bladings," *AIAA Paper 1990-2126*, 1990.

[43] R. Chima, "Explicit multigrid algorithm for quasi-three-dimensional viscous flows in turbomachinery," *AIAA, Journal of Propulsion and Power*, vol. 3, no. 5, pp. 397–405, 1987.

[44] A. A. Rangwalla, N. K. Madavan, and P. D. Johnson, "Application of an unsteady navier-stokes solver to transonic turbine design," *J. Propulsion and Power*.

[45] T. Katsanis, "Transonic velocities on a blade-to-blade stream surface of a turbomachine," *NASA Glenn research Center, internal paper*, 1994.

[46] E. J. Hall, "Aerodynamic modeling of multistage compressor flowfields - part2: Modeling deterministic stresses," *ASME Paper 97-GT-346*, 1997.

[47] J. D. Denton, "Calculation of three dimensional viscous flow through multistage turbomachines," *ASME Paper 90-GT-19*, 1990.

[48] I. FLUENT, "Fluent 6.1 documentation," *Manual*, 2008.

[49] R. Chima and B. Roidl, "Specific problems of non-reflecting boundary conditions," *Email correspondance*, 2008.

[50] M. Ahmadi and W. Ghaly, "A finite volume method for inviscid transonic cascade flow with solution adaptation on unstructured mesh," *CASI Journal*, vol. 44, 1998.

[51] K. Daneshkhah, "Aerodynamic inverse design of turbomachinery blading in two-dimensional viscous flow," *Ph.D. Thesis, Concordia University, Department of Mechanical Engineering*, 2007.

[52] L. Fottner, "Test cases for computation of internal flows in aero engine components," *AGARD-AR-275*, 1990. Propulsion and Energetics Panel.

[53] N. Cumpsty, *Compressor Aerodynamics*. Longman Scientific and Technical, 1989.

[54] D. G. Wilson, *The Design of High-Efficiency Turbomachinery and Gas Turbines*. MIT Press, Cambridge, Massachusetts, 1984.

[55] K. L. Gundy-Burlet, "Computation of unsteady multistage compressor flows in a workstation environment," *NASA Technical Memorandum 103839*, 1992.

[56] A. Jameson, A. Belov, and L. Martinelli, "A new implicit algorithm with multigrid for unsteady incompressible flow calculations," *AIAA Paper 94-0049*, 1994.

[57] S. Lieblein and W. Roudebush, "Theoretical loss relations for low speed two dimensional cascade flow," *NACA TN 3662*, 1956.

[58] D. Holmes and S. Connel, "Solution of 2-d navier-stokes equations on unstructured adaptive meshes," *AIAA Paper 89-1932*, 1989.

Appendix A

Validation of

Quasi-Three-Dimensional Method

The quasi three dimensional approach after [44] which was presented in chapter 2 is validated on a diverging rectangular nozzle in inviscid, subsonic flow. As the flare angle is $1.5°$ and the flow inviscid, the one-dimensional isentropic relations are used to verify the results. Figure A.1 represents the top and side view of a converging duct passage which is applied to validate the inviscid quasi 3-D code implementation. The area ratio is linearly decreasing from 1 to 0.85 and the outlet pressure ratio is 0.909. Figure A.2 presents the comparison of the axial varying pressure ratio values with the outcome computed from the 1-D theory. A good agreement can be seen where the axial pressure variation of the quasi 3-D approach is compared to the 1-D approach. Quasi 3-D approaches are very sensitive to the quality of the mesh they are applied on. Delauny meshes are ordinarily better suited for quasi 3-D computations than sheared H-meshes. Nevertheless, the E/TU-4 redesign case in chapter 4 case showed satisfying results as the mesh was set up carefully.
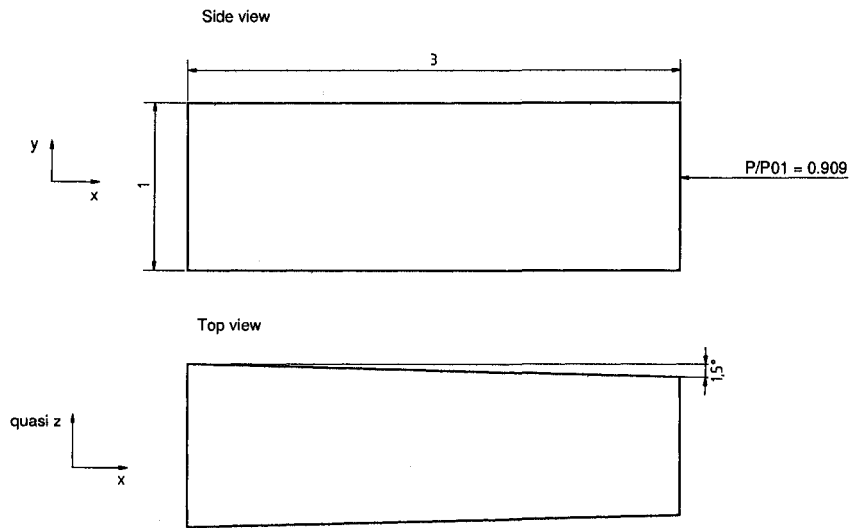
Abbildung A.1: Geometry of a converging duct passage
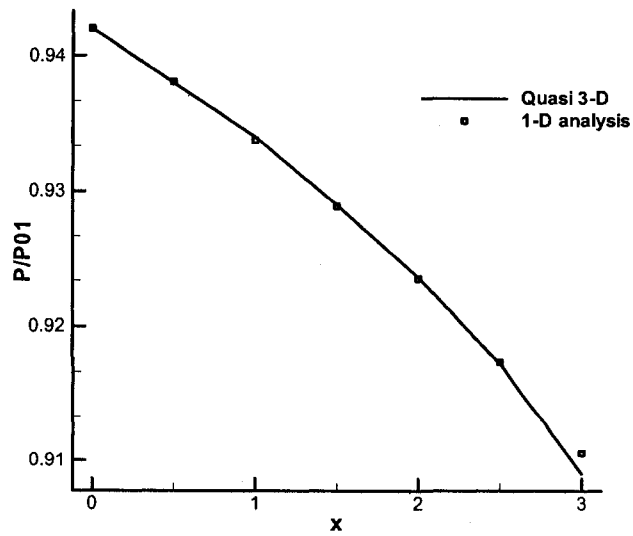
Abbildung A.2: Results of quasi 3-D and 1-D approach

Appendix B

Analysis of NRBC Models

The different approaches of non-reflecting boundary conditions, which were presented in Chapter 2, are compared and briefly discussed in this section. In section 2.7 it was already mentioned that the one-dimensional and two-dimensional, linearized Euler approach of Giles and Chima encounter problems for viscous flows at exit boundaries.

B.1. Inviscid flow

Figure B.1 depicts the pressure contours of a subsonic flow in an E/TU-4 rotor blade. The contours at inlet and exit are traveling outwards without any disturbance and the results are comparable to those developed by Giles [24]. Chima's approach is presented in Fig. B.2. The result looks similar to what was shown in Fig. B.1, however, at the in the middle of the exit boundary, the pressure wave is not properly traveling out. Chima is using exact, one-dimensional approach which is not respecting the circumferential component of the outgoing and incoming flow. The amplitude of the artificially reflected wave is $O(\theta^2)$ where θ is the flow angle. This artificially reflected wave is slightly damping the outgoing pressure contours which is clearly visible in Fig. B.2.

B.2. Viscous flow

Figure B.3 shows Giles' exact, two-dimensional boundary conditions for a subsonic case. At inlet (not shown in Figures) the pressure contours are traveling outwards without any disturbance. The reason therefore is that the entropy is assumed to be constant over the inlet boundary. That means that second order non-linearities are not disturbing the inlet boundary. At the outlet however a non-physical pressure source is clearly visible. The reason is a non-uniform entropy distribution at the outlet which is expressed in a varying velocity distribution in circumferential direction.

Chima [49] proposed to extrapolate second order terms from the interior flow to model properly the non-uniform entropy at the exit boundary. However, it is known that such an extrapolation, which deviates from the pure linearized Euler conditions at the boundary, is causing convergence instabilities in these regions. Especially Giles' exact, steady, two-dimensional non-reflecting boundaries, which are already inherently unstable (due to the inclusion of local changes of characteristic variables), might not converge.

Figure B.4 presents the same case but with Chima's one-dimensional approach. The result is again very similar to Giles' two-dimensional conditions showing also the non-physical pressure source term at the exit boundary. However, the pressure lines are less smoother near the outlet which is again due to the artificially reflected pressure waves. In Chapter 2 Chima is proposing a minor modification at the pressure term to take the non-uniform entropy at outlet into consideration. The result of this modification can be seen in figure B.5: there is no improvement in the behavior of outgoing pressure waves because the efficiency of these modifications is highly dependent on the viscous dissipation scheme (physical and artificial) and its implementation. Furthermore, the mass flow deviation at mixing plane increases substantially. In short, it can be stated that Giles' approach generally shows slightly more satisfactory results compared to Chima's approach.
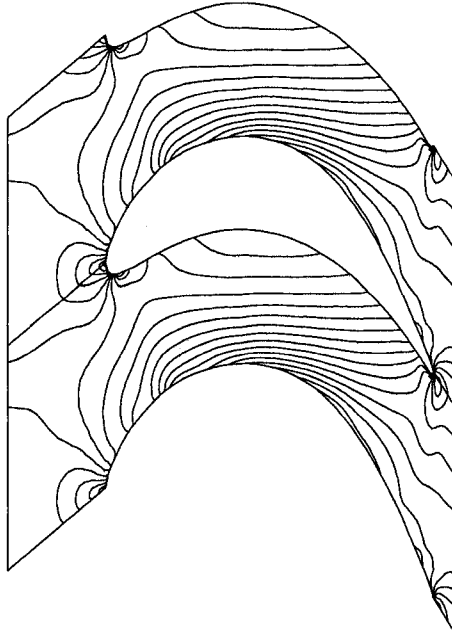
Abbildung B.1: Giles' 2-D NRBC, inviscid flow, $\Delta p/p = 0.03$
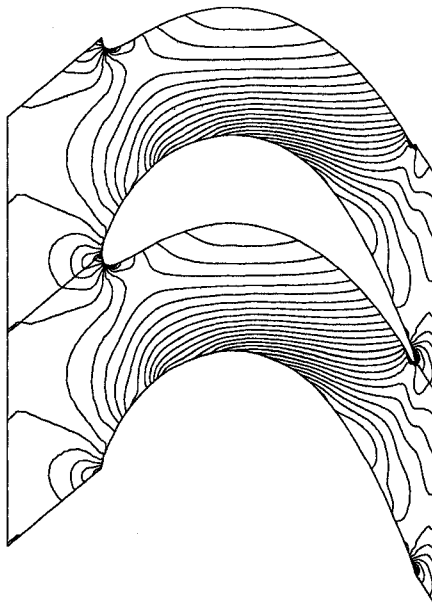
Abbildung B.2: Chima's 1-D NRBC, inviscid flow, $\Delta p/p = 0.03$
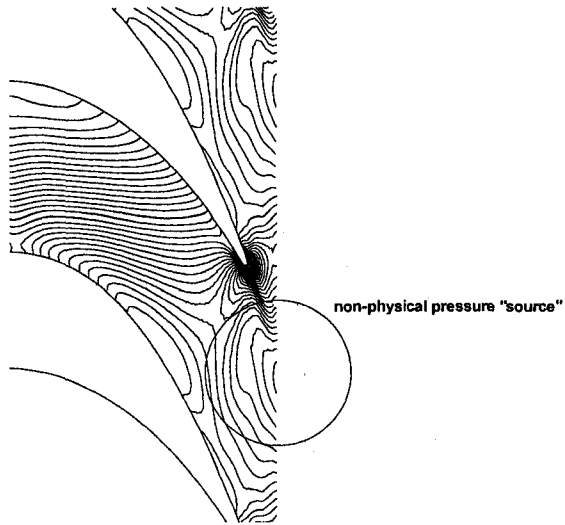
Abbildung B.3: Giles' 2-D NRBC, viscous flow, $\Delta p/p = 0.03$
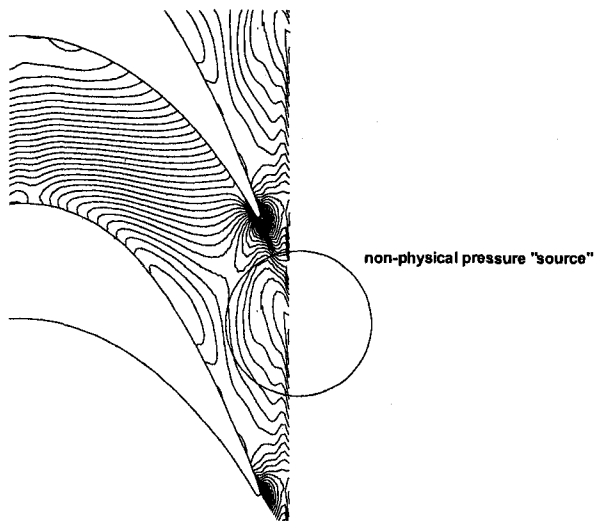
Abbildung B.4: Chima's 1-D NRBC, viscous flow, $\Delta p/p = 0.03$
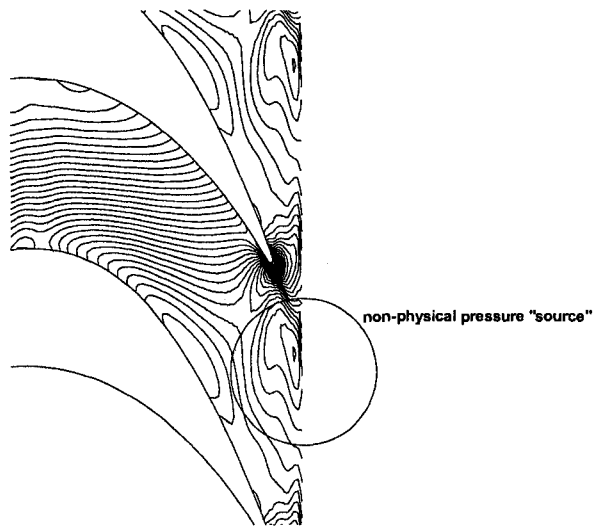
Abbildung B.5: Chima's modified 1-D NRBC, viscous flow, $\Delta p/p = 0.03$

Appendix C

Validation of CFD Multistage Code

In this appendix, the CFD multistage code described in chapter two and Appendix D is assessed for two subsonic turbine cases. The first case is the E/TU-3 turbine which was subject of investigation in chapter 4. The second case is the E/TU-4 turbine which was also already redesigned in chapter four. Both cases are simulated at design point. The blade geometries are described in [52] and enough experimental data is provided to compare numerical results with the experimental outcome.

C.1. E/TU-3 Analysis Validation

The E/TU-3 single stage turbine was validated by comparing the simulation results with available experimental data such as the rotor flow angles, rotor average inlet velocities, and stage efficiency. Tables C.4 and C.5 list the geometric characteristics of the turbine stator and rotor, and the stage design point conditions, respectively.

A hybrid mesh was applied for both stator and rotor regions. An unstructured mesh using Delauny triangulation was used for the interior flow field and an unstructured O-mesh was constructed around the blade surface so as to properly resolve the

boundary layer and to ensure that y+ < 1 near the blade surface. The stator and rotor foreground meshes consisted of 9842 nodes (19266 cells) and 9659 nodes (18904 cells), respectively. The background meshes which were required by the turbulence model had 6800 nodes (13182 cells) for both blade rows. A poor grid quality near stator outlet or rotor inlet plane can lead to substantial deviation in corrected mass flow rate at the mixing plane.

A converged solution, would have a discrepancy in the corrected mass flow rate around 0.03% at the mixing plane. A close up of the mesh in the rotor LE and TE regions is given in Fig. C.1. The results obtained from the analysis mode are compared with the experimental values observed at midspan in Table C.6. The deviation in flow velocity between numerical and experimental value may be caused by the slight discrepancy in mass flow rate at midspan as the 2D solution considers only the average mass flow over the duct height. The experimental mass flow rate might be slightly higher than the average level at midspan. In order to approximate the endwall boundary layer growth 3-D numerical results were consulted. The effect of blockage in this particular case is substantially contributing to the solution and should not be underestimated. For a quasi 3D stage simulation the results were rather accurate.

C.2.   E/TU-4 Analysis Validation

The entire E/TU-4 turbine consists of four stages. The flow through this turbine is subsonic and well behaved, i.e. attached. While the shape of the stator blades does not vary much in the span-wise direction the rotor blades are highly twisted and leaned. In this section, the midspan sections of the first 2.5 stages were considered, and the second and third stators were redesigned. A sheared H-mesh was used to model the blade row passages where the first and last blade rows consist of 8500 nodes (18522
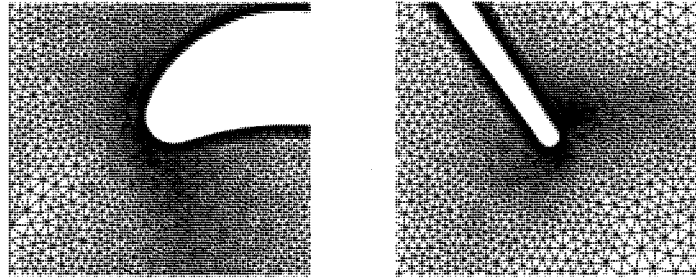
Abbildung C.1: Mesh close-up near LE and TE

cells). The second, third and fourth blade rows were meshed with 6500 nodes (12642 cells). The variable tip radius was taken into account in the flow calculations, however, end-wall boundary layer growth in the axial direction was again not considered as its prediction is known to be complex.

The results obtained from the analysis mode are compared with the experimental values in Table C.6. The outlet boundary conditions of the the third stator (5th blade row) where adjusted to match the inlet flow conditions given in the experimental data at first stator inlet (see Table C.5).

Stator inlet flow angles were matched rather well, however, the absolute velocities and static pressure ratio were comparatively off. These deviations are mainly caused by the pronounced 3D effects that affect the mid-span section as the blade aspect ratio is just around 2.6 and the rotor blades are highly twisted. Moreover the 3D losses that occur in an experimental multistage turbine such as end-wall losses, tip-clearance losses, secondary flow losses and 3D mixing losses, cannot be accounted for in a 2D multistage design.

Tabelle C.1: E/TU-3 stage geometric characteristics

	Stator	Rotor
Inlet blade angle β_1	0°	45°
Outlet blade angle β_2	67°	54.5°
Number of blades	20	31
Stagger angle	45°	33°
Pitch to chord ratio	0.65	0.66
Aspect ratio	1.92	1.22
Axial gap to stator chord	0.57	
Nominal inlet M_{abs}	0.20	0.84
Nominal exit M_{abs}	0.84	0.4
Nominal inlet M_{rel}	-	0.45
Nominal exit M_{rel}	0.45	0.69

Tabelle C.2: E/TU-3 design point conditions

Stator inlet T_0	346 K
Stator inlet P_0	1.97 bar
Rotor speed	7800 rpm
$\dot{m}_{corrected}$	97 $(kg \cdot K)/(s \cdot kg)$

Tabelle C.3: E/TU-3 analysis scheme assessment

	Measured	Computed
$\alpha_{2,stator}$	-68.3°	-67.9°
$\alpha_{2,rotor}$	-55.2°	-55.34°
$\alpha_{1,rotor}$	44.7°	44.5°
inlet flow velocity, rotor [m/s]	151.8	153.9
η_{isen}	89.9%	88.2% (quasi 3D)
Total pressure ratio	1.77	1.78

Tabelle C.4: E/TU-4 multistage geometric characteristics

	Stators 1-3	Rotors 1-2
β_1	15°	50°
β_2	71°	72.5°
Pitch to chord ratio	1.568	1.458
Aspect ratios	2.38, 2.66, 2.88	2.55, 2.77
Axial gap to stator chord	0.11	0.21

Tabelle C.5: E/TU-4 design point conditions

Stator 1 inlet T_o	405 K
Stator 1 inlet P_o	2.60 bar
Rotor speed	7500 rpm
Mass flow rate	7.5 kg/s

Tabelle C.6: E/TU-4 analysis scheme assessment

	Measured (3D)	Computed (2D)
S1 inlet Mach number	0.161	0.152
S2 α_1	90.0°	97.7°
S2 inflow velocity, [m/s]	79.0	70.1
S3 α_1	-93.0°	95.3°
S3 inflow velocity, [m/s]	85.1	72.3
Δp at S3 inlet $[p_5/p_{01}]$	0.43	0.39

Appendix D

Flow Solver Details

In this appendix, the implementation and solution of the governing equations in a time marching scheme is presented. In order to maintain a stable flow calculation and to capture discontinuities, artificial terms were implemented. An explicit Runge-Kutta time-stepping procedure is employed to receive a steady state solution.

D.1. Integration to steady State

The discretization of the spatial derivatives transforms Eq. 2.8 into the set of coupled ordinary differential equations

$$\Omega_i \frac{dU_i}{dt} + [Q(U_i) - D(w_i)] = 0 \quad i = 1, 2, 3, ..., n \tag{D.1}$$

where n is the number of mesh nodes. The residual $Q(U)$ represent the discrete approximation to the convective fluxes. $D(U)$ represents the dissipative and body force terms, i.e. the discrete approximation to the viscous fluxes, the artificial dissipation terms as well as the quasi 3-D related source term. These equations are integrated in

pseudo-time using a five-stage hybrid time-stepping scheme given by

$$
\begin{aligned}
U^{(0)} &= U^n \\
U^{(1)} &= U^{(0)} - \alpha_1 \frac{\Delta t}{\Omega} \left[Q(U^{(0)}) - D_0 \right] \\
U^{(2)} &= U^{(0)} - \alpha_2 \frac{\Delta t}{\Omega} \left[Q(U^{(1)}) - D_1 \right] \\
U^{(3)} &= U^{(0)} - \alpha_4 \frac{\Delta t}{\Omega} \left[Q(U^{(2)}) - D_2 \right] \\
U^{(4)} &= U^{(0)} - \alpha_4 \frac{\Delta t}{\Omega} \left[Q(U^{(3)}) - D_3 \right] \\
U^{(5)} &= U^{(0)} - \alpha_5 \frac{\Delta t}{\Omega} \left[Q(U^{(4)}) - D_4 \right] \\
U^{n+1} &= U^{(5)}
\end{aligned}
\tag{D.2}
$$

where

$$
\begin{aligned}
D_0 &= D_1 = D(w^{(0)}) \\
D_2 &= D_3 = \beta \, D(w^{(2)}) + (1 - \beta) \, D(U^{(0)}) \\
D_4 &= \gamma \, D(U^{(4)}) + (1 - \gamma) \, D(w^{(2)})
\end{aligned}
\tag{D.3}
$$

U^n represents the value of the solution vector at the nth time step and $U^{(q)}$ represents the values at the qth stage within a time step. The dissipative operator $D(U)$ is evaluated only at the first, third, and fifth stages of the scheme, and is employed to construct the subscripted D_q operator which represents a linear combination of present and previous evaluation of $D(U)$. This scheme represents a particular case of a large class of multi-stage time-stepping schemes where the coefficients are chosen in order to maintain good stability properties when the viscous terms are dominant, and to ensure large damping of high-frequency errors. The values of these coefficients are taken as

$$
\beta = 0.56 \quad \gamma = 0.44
$$

97

and

$$\alpha_1 = 1/4 \quad \alpha_2 = 1/6 \quad \alpha_3 = 3/8 \quad \alpha_4 = 1/2 \quad \alpha_5 = 1$$

D.2. Artificial dissipation

In principle, the physical viscous terms of the Navier-Stokes equations are capable of providing the numerical scheme with the dissipative property necessary for stability and capturing discontinuities. However, for high Reynolds-number flows, this can only be achieved by resorting to extremely small mesh spacing throughout the domain. Thus, in practice, it is necessary to introduce artificial dissipative terms to maintain stability in the essentially inviscid portion of the flow field, and to efficiently capture discontinuities. These additional dissipative terms must be carefully constructed to ensure that the accuracy of the scheme is preserved both in the inviscid region of the flow field where the convective terms dominate, as well as in the boundary layer and wake region where the artificial dissipation terms must be much smaller than the physical viscous terms. Previous Navier-stokes solutions on highly stretched meshes have demonstrated the need for different scaling of the artificial dissipation terms in the streamwise and normal directions within the regions of viscous flow. However, for unstructured meshes, directional scaling is significantly more difficult to achieve since no mesh coordinate line exist. In fact, unstructured meshes have traditionally been considered to be truly multi-dimensional isotropic constructions with no preferred direction. However, as stated perviously, the efficient solution of high-Reynolds-number viscous flows requires the meshes with highly stretched elements in the boundary layer and wake region, since the physical phenomena are highly directional in nature. For such meshes, even in the unstructured case, a direction and a magnitude of the stretching can be defined for each mesh point. This stretching vector, denoted as s need not necessarily line up with any of the mesh edges. If the mesh is directly derived from

98

structured quadrilateral mesh by splitting each quadrilateral into two triangles, the stretching magnitude and direction may be taken as the aspect ratio and the major axis of the generating quadrilateral element for each triangular element respectively. In more general cases, the generation of directionally stretched unstructured mesh requires the definition of local stretching factors throughout the flow field. These can in turn be used to scale the dissipation terms. It is important to note that these stretching vectors represent grid metrics which do not depend on the flow solution.

The artificial dissipation operators on unstructured meshes has previously been constructed as a blend of an undivided pseudo-Laplacian, proposed by Holmes and Connel [58], and biharmonic operator in the flow field. The pseudo-Laplacian for a node is given by

$$\nabla^2(U_i) = \sum_{k=1}^{n} w_{k,i}(U_k - U_i) \qquad (D.4)$$

where k represent all neighbors of node i. The weights $w_{k,i}$ are chosen such that the pseudo-Laplacian of a linear function will be zero, as would be the case for true Laplacian. These weights are defined as

$$w_{k,i} = 1 + \Delta w_{k,i} \qquad (D.5)$$

where $\Delta w_{k,i}$ are computed as

$$\Delta w_{k,i} = \chi_{x,i}(x_k - x_i) + \chi_{y,i}(y_k - y_i) \qquad (D.6)$$

where

$$\chi_{x,i} = \frac{(I_{xy}R_y - I_{yy}R_x)_i}{(I_{xx}I_{yy} - I_{xy}^2)_i}$$
$$\chi_{y,i} = \frac{(I_{xy}R_x - I_{xx}R_y)_i}{(I_{xx}I_{yy} - I_{xy}^2)_i} \qquad (D.7)$$

in the above equations R and I represents the first and second moment of inertia of the control volume in each coordinate direction, that is:

$$
\begin{aligned}
R_{x,i} &= \sum_{k=1}^{n}(x_k - x_i) \\
R_{y,i} &= \sum_{k=1}^{n}(y_k - y_i)
\end{aligned}
$$

(D.8)

and

$$
\begin{aligned}
I_{xx,i} &= \sum_{k=1}^{n}(x_k - x_i)^2 \\
I_{yy,i} &= \sum_{k=1}^{n}(y_k - y_i)^2 \\
I_{xy,i} &= \sum_{k=1}^{n}(x_k - x_i)(y_k - y_i)
\end{aligned}
$$

(D.9)

The biharmonic artificial viscosity term is formed by taking the pseudo-Laplacian of ∇w_i

$$
\nabla^4 U_i = \sum_{k=1}^{n}(\nabla^2 U_k - \nabla^2 U_i)
$$

(D.10)

Since the biharmonic operator may be viewed as a Laplacian of a Laplacian, the dissipation operator may be reformulated as a global undivided Laplacian operating on a blend of flow variables and their differences

$$
D(U) = \sum_{k=1}^{n}\frac{\alpha_i + \alpha_k}{2}[\kappa_2'(U_i - U_k]) - \kappa_4(\nabla^2 U_k - \nabla^2 U_i)]
$$

(D.11)

where α_i is

$$
\alpha_i = \sum_{e=1}^{n}|u_e n_{x_e} + v_e n_{y_e}| + c_e\sqrt{n_{x_e}^2 + n_{y_e}^2}.
$$

(D.12)

Physically, α_i represents the integral, over each cell i, of the maximum eigenvalue of the Euler equations in the direction normal to each cell edge. The diffusion term

becomes conservative in the U quantities if the average of α_i and α_k is taken. To ensure that the artificial dissipation is significant only in the vicinity of shocks and oscillations, κ_2' is calculated as follows:

$$(\kappa_2') = \kappa_2 \frac{\sum_{k=1}^{n}[p_k - p_i]}{\sum_{k=1}^{n}[p_k + p_i]} \tag{D.13}$$

Hence κ_2' is proportional to an undivided Laplacian of the pressure, which is constructed as a summation of the pressure differences along all edges meeting at node i. This construction has the required property of being of the order unity near a shock and small elsewhere. κ_2 is an empirically determined coefficient which is taken as 0 for subcritical flows, and as 1/2 for transonic and supersonic flows.

D.2.1 Local time stepping

Convergence to the steady-state solution may be accelerated by sacrificing the time accuracy of the scheme, and advancing the equations at each mesh point in time by the maximum permissible time step in that region, as determined by local stability analysis. Stability limitation due to both convective and diffusive characters of Navier-Stokes equations must be considered. The local time step is taken as

$$\Delta t = CFL \left(\frac{\Delta t_c \, \Delta t_d}{\Delta t_c + \Delta t_d} \right) \tag{D.14}$$

where CFL is the Courant number of the particular time-stepping scheme, and Δt_c and Δt_d represent the individual convective and viscous time-step limits respectively, the convective time-step limit for Euler equation on unstructured meshes is given by

$$\Delta t_c = \frac{\Omega}{\lambda_c} \tag{D.15}$$

where Ω denotes the area of the control volume and λ_c represents the maximum eigenvalue of the inviscid equations averaged around the boundary of the control volume, given by

$$\lambda = \sum_{e=1}^{n} |u_{AB}\Delta y_{AB} - v_{AB}\Delta x_{AB}| + c_{AB}\sqrt{\Delta x_{AB}^2 + \Delta y_{AB}^2} \qquad (\text{D.16})$$

The viscous time-step limit is taken as

$$\Delta t_d = K_d \frac{\Omega}{\lambda_d} \qquad (\text{D.17})$$

where K_d is an empirically determined coefficient which determines the relative importance of the viscous and inviscid time-step limits in the final expressions, and has taken as 0.25 in this work. λ_c and λ_d represent the maximum eigenvalue of the convective and diffusive operators, respectively, averaged about the boundary of the control volume, which for an unstructured mesh in discrete form is given by

$$\lambda_d = \frac{\gamma}{Re\,Pr\,\Omega} \sum_{e=1}^{n} \frac{\mu_{AB}}{\rho_{AB}} [\Delta x_{AB}^2 + \Delta y_{AB}^2] \qquad (\text{D.18})$$

where μ_{AB} and ρ_{AB} represent averaged values of viscosity and density along the outer edge AB of each element e.

D.2.2 Implicit residual smoothing

The stability range of the basic time-stepping scheme can be increased by implicitly smoothing the residuals. Thus, the original residuals R may be replaced by the smoothed residuals $\overline{R}$ by solving the implicit equations:

$$\overline{R}_i = R_i + \varepsilon \nabla^2 \overline{R}_i \qquad (\text{D.19})$$

at each mesh point i, where ε is the smoothing coefficient and $\nabla^2 \overline{R}_i$ represents the undivided Laplacian of the residuals which has been previously computed using the pseudo-Laplacian formulation and the geometrical weights, so that Eq. D.20 may be written as:

$$\overline{R}_i = \frac{R_i + \epsilon \sum_{j=1}^n w_{j,i} \overline{R}_j}{1 + \epsilon \sum_{j=1}^n w_{j,i}} \tag{D.20}$$

For highly stretched structured meshes, the use of individual smoothing coefficients in ξ and η mesh coordinate directions which vary locally throughout the mesh, has been found to improve significantly the convergence rate. The use of locally varying smoothing coefficients has the effect of making the scheme more implicit in the direction normal to the boundary layers, or normal to mesh stretching direction, and less implicit in the tangential direction. the implementation of the implicit residual smoothing with locally varying coefficients on unstructured meshes is accomplished by rewriting Eq. D.20 as:

$$\overline{R}_i = R_i + \varepsilon_\xi \overline{R}_{i\xi\xi} + \varepsilon_\eta \overline{R}_{i\eta\eta} \tag{D.21}$$

where ξ and η now represent the directions tangent and normal to the local mesh stretching vector, as described in the Sec. D.2. By analogy with the structured mesh, and making use a stretch vector [51], the smoothing coefficients are taken as:

$$\varepsilon_\xi = \max\left[\frac{1}{4}\left[\left(\frac{CFL}{CFL^*}\frac{1}{s+1}\phi(s)\right)^2 - 1\right], 0\right] \tag{D.22}$$

$$\varepsilon_\eta = \max\left[\frac{1}{4}\left[\left(\frac{CFL}{CFL^*}\frac{s}{s+1}\phi(s^{-1})\right)^2 - 1\right], 0\right]$$

where CFL and CFL^* are the Courant numbers of the smoothed and unsmoothed schemes, respectively, s denoted the magnitude of the stretching vector, and ϕ is

calculated from a scaling relation given in [51]. Since Eq. D.21 now contains a directionally scaled Laplacian, it can be discretized on an unstructured mesh in a manner analogous to that employed for the directionally scaled dissipation operator. For economy the resulting set of algebraic equations are solved by performing only two Jacobi iterations.

D.3. Time-accurate stepping scheme

For unsteady flow calculations, the time accuracy of the solution is obtained by means of a dual time stepping scheme, which is presented in this section. Eqs. D.1 can be discretized implicitly in time as follows

$$\frac{d}{dt}\left[U^{n+1}\Omega^{n+1}\right] + R(U^{n+1}) = 0 \tag{D.23}$$

where R is the sum of the three flux contributions, and the superscripts denote the time step of the calculation. If we discretize the time derivative term with the implicit second order Gear scheme, we obtain:

$$\frac{3}{2\Delta t}\left[U^{n+1}\Omega^{n+1}\right] - \frac{2}{\Delta t}\left[U^{n}\Omega^{n}\right] + \frac{1}{2\Delta t}\left[U^{n-1}\Omega^{n-1}\right] + R(U^{n+1}) = 0 \tag{D.24}$$

This equation for U^{n+1} is non-linear due to the presence of the $R(U^{n+1})$ term and cannot be solved directly. One must therefore resort to iterative methods in order to obtain the solution. The time integration of the discretized Navier-Stokes equations at each time step can then be considered as a modified pseudo-time steady-state problem with a slightly altered residual:

$$R^{*}(U) = \frac{3}{2\Delta t}\left[U\Omega^{n+1}\right] - \frac{2}{\Delta t}\left[U^{n}\Omega^{n}\right] + \frac{1}{2\Delta t}\left[U^{n-1}\Omega^{n-1}\right] + R(U) \tag{D.25}$$

In this case, the vector of flow variables U which satisfies the equation $R^*(U) = 0$ is the $U^{(n+1)}$ vector we are looking for. In order to obtain this solution vector, we can reformulate the problem at each time step as the following modified steady-state problem in a fictitious time, t^*

$$\frac{dU}{dt^*} + R^*(U) = 0 \tag{D.26}$$

to which one can apply the fast convergence techniques used for steady-state calculations. Applying this process repeatedly, one can advance the flow field solution forward in time in a very efficient fashion.

The time discretization of Eq. D.24 is fully implicit. However, when solved by marching in t^*, stability problems can occur when the stepping in the fictitious time t^* exceeds the physical one. This generally occurs in viscous calculations where core flow cells are much bigger than those close to solid walls. Based on a linear stability analysis, the stepping in t^* must be less than Δt^*_{max} where

$$\Delta t^*_{max} = \min\left[\Delta t^* , \frac{2CFL^*}{3CFL}\Delta t\right] \tag{D.27}$$

After limiting the time step to Δt^*_{max}, the scheme becomes stable and the physical time step Δt can be safely chosen solely on the basis of the accuracy requirement.